ATTENUATION CORRECTION IN PET USING SINGLE PHOTON TRANSMISSION MEASUREMENT

ATTENUATION CORRECTION IN POSITRON EMISSION TOMOGRAPHY USING SINGLE PHOTON TRANSMISSION MEASUREMENT

by:

ROBERT ANTHONY DEKEMP, B.A.Sc.

A Thesis

Submitted to the School of Graduate Studies

in Partial Fulfilment of the Requirements

for the Degree

Master of Science

McMaster University

MASTER OF SCIENCE (1992) McMASTER UNIVERSITY
(Physics) Hamilton, Ontario

TITLE: Attenuation Correction in Positron Emission Tomography using Single Photon Transmission Measurement

AUTHOR: Robert Anthony deKemp, B.A.Sc. (University of Waterloo)

SUPERVISOR: Dr. C. Nahmias

NUMBER OF PAGES: x, 106

ABSTRACT

Accurate attenuation correction is essential for quantitative positron emission tomography. Typically, this correction is based on a coincidence transmission measurement using an external source of positron emitter, which is positioned close to the detectors. This technique suffers from poor statistical quality and high dead time losses, especially with a high transmission source strength.

We have proposed and tested the use of single photon transmission measurement with a rotating rod source, to measure the attenuation correction factors (ACFs). The singles projections are resampled into the coincidence geometry using the detector positions and the rod source location. A nonparalyzable dead time correction algorithm was developed for the block detectors used in the McMaster PET scanner.

Transaxial resolution is approximately 6 mm, which is comparable to emission scanning performance. Axial resolution is about 25 mm, with only crude source collimation. ACFs are underestimated by approximately 10% due to increased cross-plane scatter, compared to coincidence transmission scanning. Effective source collimation is necessary to obtain suitable axial resolution and improved accuracy. The response of the correction factors to object density is linear to within 15%, when comparing singles transmission measurement to current coincidence transmission measurement.

The major advantage of using singles transmission measurement is a dramatically increased count rate. A factor of seven increase in count rate over coincidence scanning is possible with a 2 mCi transmission rod source. There are no randoms counted in singles transmission scans, which makes the measured count rate nearly linearly proportional with source activity. Singles detector dead time is approximately 6% in the detectors opposite a 2 mCi rod source.

Present hardware and software precludes the application of this technique in a clinical environment. We anticipate that real time acquisition of detector singles can reduce the transmission scanning time to under 2 minutes, and produce attenuation coefficient images with under 2% noise. This is a significant improvement compared to the current coincidence transmission technique.

ACKNOWLEDGEMENTS

I would like to gratefully acknowledge the support and inspiration of my mentor Dr. Claude Nahmias. He assisted me greatly in maintaining steady progress during the course of this work, and also in communicating the results clearly through the writing of this document.

I am also grateful for the help given by John Young at SIEMENS/CTI, which enabled me to implement the data acquisition on the McMaster ECAT PET scanner.

Finally, I thank all those in the MIND lab at the McMaster University Medical Centre who helped make this project not only a fruitful scientific endeavour, but an enjoyable experience as well.

TABLE OF CONTENTS

LIST OF TABLES

LIST OF ILLUSTRATIONS

INTRODUCTION

In Vivo Techniques in Nuclear Medicine

The ability to study metabolic processes in vivo is unique to Nuclear Medicine. Tracer amounts of pharmaceutical compounds are labelled with radioactive isotopes and administered into the body. Planar imaging can be done using a gamma camera. Tomographic sections through the body can be performed with SPECT imaging where a gamma camera is rotated around the patient to obtain information at multiple views. Positron Emission Tomography (PET) is another instrument which measures the distribution of activity using a planar ring of detectors around the patient. Tomographic images can then be reconstructed. It is easily the most sensitive nuclear medicine imaging instrument and has the greatest potential to measure quantitative metabolic rates.

Important metabolic measurements include brain blood perfusion, glucose and dopamine utilization. Measurements of regional cerebral blood flow are used in activation studies to examine changes in the distribution of perfusion, related to specific mental or physical tasks. Regional cerebral metabolic rate as measured by the fluoro-deoxy-glucose (FDG) method, is an important diagnostic tool for diseases such as Huntington's Chorea, where the striatum has decreased uptake. Parkinson's disease is

manifest in reduced striatal uptake after injection of fluoro-L-dopa. L-dopa is a precursor to dopamine which is an essential neurotransmitter in the brain. Alzheimer's disease often results in significant atrophy of the brain cortex, which is visible with an FDG scan. Labelled ammonia and FDG can also be used to assess the viability of ischemic heart tissue in patients who have had myocardial infarction. Various chemicals used in the treatment and diagnosis of schizophrenia are also being investigated using PET. Positron tomography is the only, accurate method of measuring regional metabolic rates in vivo.

History of Positron Emission Tomography

In 1951 W.H.Sweet proposed the use of positron emitters for diagnostic imaging of brain tumours. F.W.Wrenn et al. independently published similar ideas in the same year, but it was Brownell and Sweet who built the first positron scanner in 1953. They were able to obtain a lateral projection image of brain tumours using ^{74}As. Some gross left/right position information was available as well with this scanner. The first tomographic scanner was built in 1962 at the Brookhaven National Laboratory by S.Rankowitz et al. It was a 32 crystal ring of detectors which imaged a single plane of the head, but had very limited display capabilities. It was not until the 1970s when image reconstruction was implemented for X-ray CT scanning, that suitable image reconstruction and display techniques became available for such PET scanners. Since that time many advances have been made in image resolution, sensitivity, detector design and image processing. Today over 200 research centres worldwide have

positron emission tomographs which are used to investigate biochemical functions.

Quantitative Accuracy

The research in PET instrumentation and processing has resulted in many scanners being custom built at various research centres. As well, several commercial companies market scanners which embody the latest developments. These systems typically employ block detectors of Bismuth Germanate (BGO), and can image several centimetres of the body in multiple tomographic sections. Image resolution is typically 5 mm, and the section thickness is 5 mm as well. This provides an isotropic sampling in a volume of tissue up to 50 cm by 50 cm transaxially and 15 cm axially.

Images can be quantified to absolute concentrations of radioactivity [Bq/cc], to an accuracy of approximately 5% if appropriate calibrations and corrections are performed. Tracer kinetic modelling is necessary to convert radioactive concentration to absolute physiological units or metabolic rates. However, this is not a simple matter. It requires blood samples to be drawn during the study and counted. The blood counts must be accurately calibrated to the scanner counts as well. Other approaches have been developed to analyze PET images which do not require absolute quantitation. These are based on repeated studies examining relative changes within a subject.

Project Scope

Positron emission tomography is based on the detection of coincident photons resulting from positron-electron annihilations. Although the ultimate goal is often to quantify metabolic activity, the primary function of PET is to determine the concentration of positron emitting isotope in a certain volume of interest. Therefore, the design of these instruments is optimized to detect the photons emitted from within the object being imaged. Attenuation of these photons causes a decreased signal to be recorded from central structures, and precludes image quantitation. It is relatively easy to implement attenuation correction using the identical (coincidence processing) design, simply by using an external source of positron emitting isotope to measure transmission of photons through the same object. However, this is not the optimal method of measuring photon transmission. It is much more efficient to measure the attenuation of the total flux of photons passing through the object. This method has not previously been investigated in positron emission tomography. The complexity of the design of hardware and software is increased over coincidence transmission measurement. It is the purpose of this work to investigate transmission measurement for attenuation correction in PET, using the detection of single annihilation photons as opposed to the detection of annihilation photons in coincidence. A prototype singles transmission technique is implemented on the McMaster PET scanner, and the performance is evaluated.

CHAPTER I

Physics of Positron Emission Tomography

Positron Emission

Many radioisotopes of chemical elements in the human body such as Carbon, Nitrogen and Oxygen decay through positron emission. This makes PET very useful in the study of chemical function and metabolic rates in vivo.

Positron Decay

Many proton rich elements can decay through positron emission. In the process, a proton is converted to a neutron and the excess charge is emitted as a positive electron (positron). All isotopes which decay this way can also balance their proton/neutron ratio through electron capture. Here the nucleus captures one of its orbiting electrons; this electron combines with a proton and it becomes a neutron. The resulting excited nucleus will then emit gamma photons as it returns to the ground state.

The reaction for positron emission is:

$$ {}_{Z}{}^{A}X \rightarrow {}_{Z-1}{}^{A}Y + \beta^{+} + \nu \qquad (1) $$

Since a positron is being emitted, an orbital electron will be lost by the atom as well, in order to preserve a neutral charge. The energy released by this process is proportional to the change in atomic mass from the parent (X) to the daughter (Y) nuclide. If m is the mass of an electron, then the lost positron and electron will account for $2 \cdot mc^2$ of this energy. The remaining energy is transferred as kinetic energy to the positron (β^+) and the neutrino (ν). Therefore, the positron kinetic energy covers a continuous spectrum with an endpoint energy of:

$$ E_{\beta+} = (M_x - M_y - 2m) \cdot c^2 \qquad (2) $$

This kinetic energy is lost through subsequent interactions with surrounding matter. The positron energy (Sorenson 1987) and mean range (Pages 1972) of several isotopes are shown below.

TABLE 1

PROPERTIES OF COMMON POSITRON EMITTING ISOTOPES

Isotope	Percent β^+ Decay	Half-life	Max Energy [MeV]	Mean Energy [MeV]	Mean Range [mm]
^{11}C	99.8	20.3 min	0.97	0.394	1.24
^{13}N	100	10.0 min	1.2	0.488	1.67
^{15}O	100	124 s	1.74	0.721	2.62
^{18}F	97	109 min	0.635	0.250	0.623
^{64}Cu	19	12.8 hours	0.656	0.258	0.656

Positron Thermalization

The principal mechanism of energy loss of ejected positrons is through inelastic collisions with atomic electrons. The positrons cause ionization and excitation of the surrounding atoms, where the energy loss of the positrons is given by:

$$\Delta E \propto M \cdot m^2 / (M + m)^2 \qquad (3)$$

The energy loss in inelastic collisions is greater for particles with small mass (M). That is why most energy is lost in electron interactions as opposed to nuclear interactions.

Elastic scattering with atomic electrons is the main mode of energy loss below the typical electron binding energy. Above this level (approximately 100 eV) electrons are inelastically scattered.

A small amount of energy is also lost through elastic scattering with atomic nuclei. The energy transferred is inversely proportional to the mass of the absorbing nucleus (Knoll 1989). Since the mass of the nucleus is large compared to an electron, little energy is transferred. This scatter does cause large angle deflections of the positron, resulting in a very erratic path traversed before reaching thermal energy.

Bremsstrahlung interactions also account for a small amount of energy loss of the positron. This results in a spectrum of X-rays being emitted up to the maximum positron energy.

Range

Elastic collisions with atomic nuclei cause large angle deflections of a positron. This means that the positron will travel a much smaller distance from its parent nucleus than the total path length travelled.

The range varies with the initial kinetic energy of the positron. These ranges have been determined for a spectrum of energies in a number of compounds (Pages 1972). Several examples are included in Table 1 for typical isotopes and materials. In tissue (or water), these positrons typically travel less than 2 mm before their energy decreases to thermal levels.

Since most energy is lost in inelastic collisions with atomic electrons, the range of the positron also varies with the number of electrons present in the medium:

$$\Delta E \propto \rho N_o(Z/A) \qquad (4)$$

where: N_o = Avogadro's number

Since Z/A (atomic number/atomic weight) is roughly constant for all elements, the energy loss depends primarily on the density (ρ) of the material. Therefore positron ranges measured in one medium can be converted to ranges in a second medium by multiplying by the density ratio of the two media.

Annihilation

When the positron energy decreases below 10 eV (thermal energy), it typically combines with an electron in an annihilation reaction. This converts the mass of the electron and the positron to energy in the form of two gamma photons. They travel in opposite directions (180° apart), at the speed of light. The two photons each have energy of 511 keV, which is the rest mass energy of an electron. Any remaining thermal energy of the positron results in a slight non-collinearity of the gamma photons. The deviation of the angles around the mean of 180° is 0.4°.

In some cases an electron can bind with the positron to form a hydrogen-like atom called positronium. This atom has a half-life of about 10^{-10} s. The common form is called para-positronium which decays through emission of two collinear 511 keV photons. A rare form, ortho-positronium, decays by emitting three lower energy photons. The positron can also react with a tightly bound atomic electron and emit a single photon of higher energy, however, this is also rare.

Gamma Ray Interactions

The end result of positron emission is typically two 511 keV gamma photons. These photons interact with the surrounding medium. There are three major interactions of gamma rays in matter: photoelectric absorption, Compton scattering, and pair production. With positron emitting isotopes, pair production is not energetically

possible. The photon energy must exceed 1.022 MeV for this effect to occur.

Photoelectric Absorption

The photoelectric effect occurs when a gamma ray interacts with a tightly bound electron. In this case the photon is completely absorbed and an electron is emitted. This photoelectron has an energy of:

$$E_{e^-} = E_\gamma - E_b \qquad (5)$$

where: E_b is the electron binding energy.

K level electrons are the most probable candidates for photoelectric interactions. After ejection of the K level electron, characteristic X-rays are also emitted as the vacant atomic energy levels are filled by the higher orbital electrons. The excited atom may alternately lose its energy by emitting an Auger electron instead of the characteristic X-rays.

The probability of photoelectric absorption increases with the atomic number (Z) of the element, and decreases with the photon energy (E_γ). One approximation which is valid at E_γ around 511 keV, is: (Evans 1982):

$$\tau \propto Z^{3.5} / E_\gamma^{3.5} \qquad (6)$$

where: τ [cm^{-1}] is the linear photoelectric absorption coefficient.

Compton Scattering

An incident gamma photon can also interact with a free electron. In this case the incident photon is scattered and transfers some of its energy to an electron in the absorbing medium. This recoil electron energy varies with the angle of scatter of the photon:

$$E_{e^-} = E_\gamma - E_\gamma' \quad (7)$$

$$E_\gamma' = 511/(2 - \cos\theta) \text{ [keV]} \quad (8)$$

where: $E_\gamma = 511$ [keV]
θ = the scattering angle

The Compton scatter distribution is strongly forward peaked at 511 keV. The Compton scatter coefficient (σ [cm^{-1}]) depends on the number of electrons available as scattering targets, and therefore increases linearly with increasing density of the medium (Knoll 1989).

Linear Attenuation Coefficient

Intensity of a monoenergetic, well-collimated beam travelling through a uniform medium follows a decreasing exponential relation:

$$I = I_o e^{-\mu x} \quad (9)$$

where: I = Intensity of the beam at distance x through the medium
I_o = Initial beam intensity
x = distance travelled through the medium [cm]
μ = attenuation coefficient [cm^{-1}]

For 511 keV photons the attenuation coefficient is simply the sum of the photoelectric absorption coefficient τ, and the Compton scatter coefficient σ, i.e. $\mu = \tau+\sigma$.

Another useful characterization of attenuation is the half-value-layer (HVL). This is the thickness of absorber needed to reduce the beam intensity by a factor of two, i.e. HVL = 0.693/μ. The attenuation coefficients for 511 keV photons are shown below for several absorbing media (Evans 1982, Johns 1971).

TABLE 2

ATTENUATION PROPERTIES OF SOME COMPOUNDS

Medium	ρ [g/cm^3]	μ [cm^{-1}]	HVL [cm]
Air	0.0013	0.00011	6300
Water(≈Tissue)	1.00	0.095	7.3
Lead	11.3	1.6	0.43
Aluminum	2.7	0.22	3.2

In PET the gamma ray flux incident on the detectors is rarely collimated. A spatially distributed source produces photons which are incident on a given detector from many different angles. The photons are also scattered within the source, and between the detectors themselves. This is called broad beam geometry and causes a higher signal to be recorded than in the narrow beam case described above. The acceptance of some scattered photons will cause the apparent attenuation coefficient to be decreased.

Media Density

The density of the attenuating medium is the major factor governing the distribution of energy released by positron emitting isotopes. The effective atomic number (Z) of an absorbing medium is the principal determinant of its density. The three main effects are:

1. Range of positrons decreases linearly with Z.
2. Photoelectric absorption coefficient increases as $Z^{3.5}$.
3. Compton scatter coefficient increases approximately linearly with Z.

The range of positrons in the source being scanned will affect resolution of the images produced. Compton scatter and absorption of gamma photons within the extent of a source will result in decreased signal from those areas. Density is also important in detector design, where a high probability of photoelectric absorption is desired.

Detectors

It is necessary to record the position, time and energy of the 511 keV gamma photons to perform positron emission tomography. Detectors are typically designed to optimize one or more of these measurements. Several options currently exist, but by far the most common is to use a scintillation detector called BGO (Bismuth Germanate). Bismuth (Z=83) has a high probability of photoelectric absorption, which is necessary to detect the photons. Other scintillation detectors used include Thallium activated Sodium Iodide (NaI(Tl)), which has better energy resolution than BGO. Barium Fluoride (BaF) is used in time-of-flight PET systems because it has very good timing capability.

Other detection devices such as multiwire proportional counters are used as well because they can be constructed to produce excellent positional information. In this system, a converter shield is used to absorb the gamma photons and emit photoelectrons. Some of these electrons escape into the converter holes and are drawn towards the multiwire grid where their position and time are encoded. The converter shield can be designed to select the photon energy of interest.

Semiconductor detectors have a narrow energy gap between the valence band and the conduction band. Electrons can be excited into the conduction band and can produce an output current. Compton and photoelectric interactions generate electrons that can produce this effect. However, the probability of this is low due to the typically small size of these detectors.

Pulse Processing

In order for photon interactions to be recorded, electronic signals are generated and then analyzed to determine the time of arrival of the photon, as well as its energy and position.

Timing

The pulse signals can be generated by a number of methods. These include photomultiplier tubes (PMTs) coupled to scintillation detectors, and gas-filled chambers used with multiwire systems. The signal may also come directly from a semiconductor detector. In general the signal rises to a peak amplitude and then decays back to a background level. The most accurate timing information is generated by systems with fast and consistent rise time with large amplitude and little noise in the signal.

The time of arrival of a photon is determined by the time when the pulse rises above some threshold voltage level called a trigger. Variability in signal amplitude for the same shape pulse will cause amplitude walk in the timing. Noise in the signal will cause a statistical uncertainty called time jitter. Inconsistent rise time for a given amplitude signal will cause rise time walk in the timing.

The performance of scintillator-PMT systems are generally determined by the characteristics of the scintillation detector and not by the PMTs. Gas-filled chambers

generally have slower and inconsistent rise time, and therefore poorer timing resolution.

Dead Time

There is a minimum period within which only one event can be counted. This is called the dead time (τ) of the system. Dead time may result from processes within the detector itself or in the associated electronics. When multiple photons arrive at a detector within a time shorter than the system dead time, one or more of them will not be counted. Photons which are not counted because of this effect are referred to as dead time losses.

There are two common models of dead time behaviour, paralyzable and nonparalyzable systems. In paralyzable systems, if a photon strikes the detector within the dead time of a preceding event, the dead time is extended by a time τ following the second photon, even though it is not counted. The model describing this behaviour is given as:

$$m = ne^{-n\tau} \qquad (10)$$

where: m = measured count rate
n = true count rate
τ = dead time

In the nonparalyzable case, a second photon striking the detector within the dead time interval is not counted, but is assumed to have no effect on the detector and does not extend the dead time. The equation describing this effect is:

$$n = m / (1 - m\tau) \quad (11)$$

The measured count rate will actually decrease in paralyzable systems if the true rate is increased beyond the value of $1/\tau$, eventually paralyzing the system. Nonparalyzable systems rise to a constant measured rate which equals $1/\tau$ at high true rates. With low dead time losses the two systems produce practically equivalent measured count rates.

At high count rates, pulses generated by the detection system may overlap. This phenomena is called pulse pile-up. Overlapping pulses have altered amplitudes which affect the energy discrimination. Therefore pulse pile-up affects the spectrum or the apparent energies of the photons, depending on count rate.

Energy Discrimination

Energy discrimination is employed principally in scintillation detector systems. The light in the detector crystal is converted to an output voltage by the PMT. The amplitude of this signal is proportional to the energy of the photon absorbed by the detector. Discriminator circuits are used to accept or reject photons within a desired energy range. The photons of interest in PET are of course at 511 keV. Scattered photons arrive at lower energy and can be rejected if they are below the lower discriminator setting. The settings chosen depend on the energy resolution of the

detectors. There are many factors which affect energy resolution such as light output of scintillation detectors, pulse shape and noise.

Position Encoding

It is necessary to know the spatial origin of the photons that have been recorded. In some systems this is a simple task because each detector may produce its own output signal. However, in many cases there are fewer signals than there are detector locations, and signals are combined to deduce the location of the photon interaction.

For example, in most gamma cameras relatively few PMTs are used to spatially encode one large crystal of NaI into a matrix of 256 by 256 pixels. In multiwire PET the X and Y coordinates are given by the position of the wires where the electron charge is collected. In most modern positron tomographs block detectors are coupled to multiple PMTs to produce a rectangular matrix of detector locations. The detector itself may also have elaborate light guides cut into the crystal. This modifies the PMT signals depending on the spatial origin of the photon interaction within the block.

Coincidence Counting

The result of positron emission is typically two 511 keV photons emitted in opposite directions. PET is based on the measurement of these coincident photons, which arrive at two detectors at nearly the same instant in time. There are three types of coincidences which are measured: prompt (true), random and scattered.

Time Spectroscopy

It is necessary to determine the time interval between arrival of photons in positron tomography. A time to amplitude converter (TAC) is used to convert the time interval between two pulses into an output voltage. Consider a circuit with the timing signal of one detector connected to the start input of a TAC, and the timing signal of another detector sent through a fixed delay of length T and then to the stop input of the TAC. When a positron emitting isotope is placed between the detectors, pairs of prompt (coincident) photons are produced. Some of these pairs will strike the detectors at (nearly) the same time. Ideally if both detectors absorbed one of the photons at the same instant, the TAC would output a voltage corresponding exactly to the delay T. However, due to time jitter and walk of the detector electronics, the output voltage actually forms a distribution of values centred about the time T. The distribution represents the timing uncertainty of the system. The time resolution (τ) is commonly given as the full width at half maximum (FWHM) of this distribution.

Prompt Coincidences

Coincidence events are typically counted by connecting the detector circuits directly to a coincidence circuit which generates an output signal whenever two pulses are received within a given time interval. The interval is chosen to include the distribution of prompt events created by the timing uncertainties of the electronics. It is therefore larger than the time resolution of the system e.g. 2τ, and is called the coincidence time window (τ_c). The coincidence window must also be wide enough to include any timing differences resulting from distance travelled by the photons. For example an annihilation event occurring adjacent to one detector will result in a 2 ns delay between the two photons, if the second detector is 60 cm away. Typical coincidence time windows vary from 4 to 20 ns in PET. There is also a small chance that more than 2 photons will be detected within the coincidence window. When this occurs a multiple coincidence is recorded. Multiple coincidences do not contribute to the measured signal, but do affect the dead time of the system.

Randoms

There are also pairs of photons which are recorded as coincidence counts but which did not come from the same annihilation event. These photons arrive at random time intervals, some of which may be less than the coincidence window. The random coincidences counted as a result of this process form a constant background over which the prompt coincidences are measured. In fact the randoms count rate is given as:

$$R = \tau_c r_1 r_2 \qquad [\text{cps}] \qquad (12)$$

where: τ_c = coincidence time window
r_1 = single photon count rate at detector 1
r_2 = single photon count rate at detector 2

Scatter

With the coincidence circuit described it is impossible to determine if one or more photons have been Compton scattered before arriving at a detector. 511 keV photons scatter with a Compton angle that is quite severely forward peaked, as described by eq.(8). A photon scattered through an angle of 30° still has an energy of 450 keV. This is much higher than the typical lower energy discriminator setting used in positron tomography. This scattering angle can easily cause a recorded event to be mispositioned by 5 to 10 cm in a 60 cm field of view (FOV). Therefore the prompt coincidences measured include both scattered and unscattered photons.

Unscattered photons originating from the same annihilation event which are recorded by the coincidence circuits are referred to as true events. These are the events of interest; they are proportional to the regional isotope concentration.

CHAPTER II

Quantitation in PET

Tomographic Image Reconstruction

When an event is recorded in coincidence by a pair of detectors, it is assumed that an annihilation occurred somewhere along the line joining the two detectors. This line is referred to as a line of response (LOR). When detectors are arranged in a planar ring around a source of positron emitting isotope, many line integrals along these LORs can be sampled. A parallel set of line integrals measured at a given angle is called a projection. Theoretically the inverse Radon Transform can be used to create cross sectional images of the distribution of radioactivity, if an infinite number of projections are measured in a plane through the object (Barrett 1984).

Detector Geometry and Sampling

With a planar ring of detectors, each detector may be able to record coincidences with a set of opposing detectors as shown in Figure 1. The lines connecting the pairs of detectors form a fan beam of LORs, which is also called a

profile or view measured at a given angle or at a given detector. If planar projections are measured at many angles around an object of interest, then a tomographic image of the measured property can be reconstructed. This image is an approximation of the true distribution since only a finite number of projections can be measured. In fact both the attenuation distribution and then the distribution of radioactivity are measured during a typical PET study.

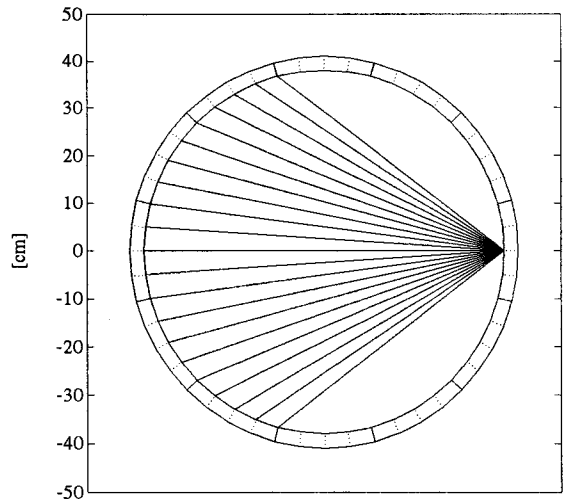

Figure 1 - Coincidence Fan Beam

Circular configurations of detectors are the most geometrically efficient, and are by far the most common today. There are however, many variations in the number of detectors within a ring, the ring diameter, and the ring spacing in multiplanar systems. The sampling distance is an important measure of the geometry of a tomograph. If all measured LORs are drawn within a ring of detectors, concentric circles are produced with the LORs tangent at different points. The distance between these circles is the

sampling distance. It is equal to half of the detector width at the centre of the field of view (FOV), and decreases radially. The major factor affecting the resolution of PET scanners is the sampling distance, and therefore the detector size. The smaller the detectors, the more LORs which are created and the better the resolution of the resulting images.

Coincidence Sinograms

Lines of response can easily be defined according to their angle (θ), and radial distance (r) from the centre of the field of view. It is common to store the projections ($p(r,\theta)$) recorded along these LORs in a matrix called a sinogram. Each point in the matrix corresponds to a pair of detectors. For example, there may be 400 detectors around a ring, where each detector may form coincidences with the opposing 150 detectors. The radial axis (abscissa) of the sinogram could be 150 detectors wide, and the angular axis (ordinate) would then be 200 detectors high. In this case there are half as many angles as there are detectors because one LOR is duplicated in the fan beams of each pair of detectors. The term sinogram is coined from the observation that a point source which is off-centre in the FOV, produces counts in LORs which trace a sine wave in the data matrix. A point source in the centre of the FOV traces a thin vertical line centred horizontally in the matrix.

Reconstruction from Projections

Image reconstruction is based on the measurement of many projections $p(r,\theta)$ through an object. In PET, the projection is actually a line integral of the concentration of radioactivity, i.e.

$$p(r,\theta) = \int c(x,y)\, ds \quad \text{where } s \perp r \tag{13}$$

Various methods of backprojection into a rectangular image space have been developed. In the simplest case, the counts in a given projection are added to all pixels along the projection line, i.e.

$$\hat{c}(x,y) \propto \int p(r,\theta)\, d\theta \tag{14}$$

$$\propto \Sigma\, p(x\cos\theta + y\sin\theta,\ \theta)$$

A less noisy image is obtained with a variation of this technique. The projection and image data can be related using Fourier Transforms. A method known as convolution backprojection first convolves the projections with a filter function before summation. The convolution filter results basically from a change of variables from rectangular to polar coordinates within the Fourier Transform (Herman 1979). Unfortunately the convolution results in ringing artifacts in the image due to the finite number of samples. Various filter windows are typically implemented to smooth this effect. Convolution backprojection is the most widely used method in commercial systems because it is fast and easy to implement, and performs well when good quality projection data have been acquired (Herman 1980).

There is also much interest in iterative reconstruction methods. These techniques start with an initial estimate of the image distribution. The corresponding projection data is then calculated (forward projected). Based on the difference between the measured and calculated projections, the calculated projections are altered and a new image distribution is backprojected. This procedure continues in a loop until the measured and calculated projections are sufficiently close. It is very difficult to determine when to stop the iteration, based on the difference in the projection data or based on the resulting image quality. If the stopping rule is not chosen appropriately the image quality can actually degrade as more iterations are computed. To date, the computational effort required to perform these reconstructions has not resulted in a concomitant increase in image quality.

Performance Measures

There is a standard set of criteria which is used to determine the quantitative imaging characteristics of a positron emission tomograph. This includes measures of resolution, count rate performance, image uniformity and stability of the system.

Transaxial Resolution

Transaxial resolution is typically quoted as the full width at half maximum (FWHM), and the full width at one tenth maximum (FWTM) of the point spread

function. It is easily measured by imaging a point source of radioactivity. The resolution is measured both radially and tangentially from the centre of the FOV. The source is moved radially out from the centre of the field of view, and the response is measured at each location. This provides a good map of the resolution throughout the FOV. Alternately, the response to a sharp object edge can be measured to determine the resolution. As described earlier, transaxial resolution is basically a function of the tomograph geometry and the detector size.

If a resolution element contains two structures with different concentrations of radioactivity, then the resulting counts will have contributions from the two different regions. It is therefore impossible to determine what the absolute concentration is in one structure or the other. This phenomenon is called partial volume averaging.

Objects which are smaller than approximately twice the FWHM resolution of the tomograph are not measured accurately. A small point source results in a measured concentration which is lower than the true value. This is simply due to the smoothing effect of the point response function. A point source in the FOV will produce an image of the point response function, and similarly any other object produces an image which corresponds to the true object distribution convolved with the point response function. The converse is true when a non-radioactive object is surrounded by radioactivity. If the object is too small, a count rate of zero will not be recorded because of the contribution from the adjacent regions.

Axial Resolution

Axial Resolution is a measure of the point spread function in the axial direction. This is typically the spread of the measured counts across transaxial images. If a thin source of radioactivity is mounted parallel to the tomographic imaging planes, the axial resolution can be measured. The source is initially positioned at the axial edge of the field of view, and centred radially. It is then moved in small increments axially into the FOV, recording the total counts in each plane at every source position. The counts will rise and fall in certain image planes as the source moves through the axial FOV. Once the source has travelled through the entire FOV, the FWHM and FWTM can be computed for each plane from the recorded axial profiles. This process can be repeated with the source positioned at different radial distances from the centre of the FOV. As with transaxial resolution, the step response at an object edge can be measured to determine the axial resolution.

Count Rate

It is necessary to determine the maximum count rate at which a tomograph can function. Systems with a higher count rate capability can form images in a shorter time, and therefore monitor dynamic processes within the body. A decaying source of known strength is positioned in the FOV, while successive acquisitions are performed. The measured counts are then plotted against source strength to determine the response. Typically, the total prompt coincidences, randoms, multiples and singles are recorded.

The principal determinants of the count rate response are the detector design and the dead time characteristic of the system, which follows either a paralyzable or nonparalyzable model.

Efficiency

An important measure of a detector's performance is its intrinsic efficiency. This is simply the ratio of the number of recorded counts, divided by the total number of photons incident on the detector. The detector material and the dead time losses are the two principal factors determining intrinsic efficiency.

Uniformity

Uniformity refers to the degree of fluctuations in an image of a known uniform object. Such fluctuations come from the statistical distribution of recorded coincidences in space and time. The relative standard deviation of a region with a known uniform property will approach zero as the number of recorded counts increases. The number quoted is often the standard deviation divided by the region average (percent noise).

Detector malfunctions or incorrect normalization can also affect the uniformity. Images should be uniform within a given region, as well between different regions in the same object. Count rates must also be consistent between successive scans of the

same object.

Statistical Image Quality

It is often desirable to create an image in which the pixels represent an absolute measure of some property of interest, that may be spatially and temporally variant. The pixel value may represent the concentration of radioactivity in a certain anatomical area or it may be a physiological measure such as blood perfusion.

There are two types of errors which affect the distribution of counts during a PET scan. The first type is systematic and results from processes which can be accurately modelled and therefore corrected. The second type is random in nature and results principally from counting statistics. Statistical noise in PET scans is affected by three random processes. The first is the noise in counting true events which are separated by random time intervals. Second, there are random coincidences which follow a statistical distribution in time and space. Third, there is a certain probability that coincidences will be Compton scattered through angles which also vary randomly.

Decay Counting Statistics

When counting disintegrations of a radioactive source, the probability of obtaining N counts in a certain time T, follows a Poisson distribution, i.e.

$$P(N) = e^{-m} \cdot m^N/N! \qquad (15)$$

where: m is the mean count obtained in time T.

The variance of the Poisson distribution is equal to the mean. For a single measurement of N if we assume that N≈m, then an estimate of the variance of N is also equal to N. In this case the estimated standard deviation of N is $\sqrt{N} = \sigma_N$.

The relative error (noise) in the measured counts can be lowered by counting for a longer time. If the count rate of the detector is stable over a measurement time kT for example, then the noise in the resulting counts will equal $\sqrt{kN}/kN$, i.e.

$$\sigma_{kN}/kN = \sigma_N/N \cdot 1/\sqrt{k} \qquad (16)$$

Therefore if we increase the counting time by a factor of k, we reduce the noise in the counts by a factor of $\sqrt{k}$.

The model described above is valid for systems which are counting a fixed proportion of the source disintegrations at all source strengths. In practice however, this is rarely the case. The detector dead time causes a lower fraction of the total disintegrations to be counted at high levels of radioactivity.

Dead Time Losses

When the system functions with dead time losses, the statistical model deviates from the Poisson distribution and the counts become more uniform. The variation of measured counts obtained with significant dead time losses is less than that described above. For the nonparalyzable system of eq.(11), the variance of the measured counts M equals (Evans 1982):

$$\sigma_M^2 = M / (1 + n\tau)^2 \quad (17)$$

$$= N / (1 + n\tau)^3 \quad (18)$$

where: n = event rate (N/T)
M = measured counts
N = dead time corrected counts

The variance of the corrected counts increases because of the high dead time losses. By using error propagation applied to eq.(11), one can obtain an estimate of σ_N^2, given σ_M^2 in eq.(18) (Kennett 1992):

$$\sigma_N^2 = \{dN/dM\}^2 \cdot \sigma_M^2$$

$$= N \cdot (1 + n\tau) \quad (19)$$

For example if the dead time losses are 50% in a nonparalyzable system, then the counting efficiency (M/N) is also 50%. The variance of the corrected counts increases by a factor of 2 because N/M = (1 + nτ). Therefore the variance of the corrected counts is inversely proportional to the counting efficiency:

$$\sigma_N^2 = N / \varepsilon \quad (20)$$

where: ε = M/N (counting efficiency)

Image Randoms

The spatial distribution of random coincidences is uniform through the entire FOV (Dahlbom 1987), while the temporal distribution varies as the source strength decreases. A higher source strength will result in a higher randoms rate as described by eq.(12).

Random coincidences must be subtracted from the total measured counts in order to be left with only prompt events. It is common in PET coincidence circuits to employ a second coincidence window of the same width as the prompt coincidence window but which is delayed by a longer time, e.g. 100 ns, in order to count randoms. It is assumed that any photon arriving within this delayed window can not be correlated with the original photon and is therefore a random coincidence. Events counted in this delayed window are subtracted from the total counts, i.e.

$$\text{Prompts} = \text{Total} - \text{Randoms} \tag{21}$$

This subtraction can be performed for every projection in real time, making the randoms correction independent of the source configuration. The noise in the delayed random coincidences is added to the noise in the total measured counts when the subtraction is performed. Therefore when comparing a high strength source with a lower strength source, the same number of prompts will be noisier when obtained with the higher strength.

Image Scatter

The scatter distribution changes with object geometry. Methods can be employed after acquisition to estimate the degree of scatter present in the counts and to remove these from the total. Assuming the randoms have been previously subtracted, one is left with only true events, i.e.

$$\text{Trues} = \text{Total} - \text{Randoms} - \text{Scatter} \tag{22}$$

This process can be a type of subtraction of average scatter profiles (Bergstrom 1980), or it may be a deconvolution of scatter point response functions (Bergstrom 1983). In this case the response of a point source in a scattering medium has been shown to decrease exponentially with distance from the source. Many other methods have been proposed, however, to date no method of scatter correction has been developed which is applicable to an arbitrary source configuration. The noise in the estimated scatter is also added to the noise in the true counts after the scattered coincidences have been removed.

Noise Equivalent Counts

In emission scanning, it is the true event count rate which is indicative of the amount of radioactivity present in a given region. With no dead time correction, the three statistical factors which affect the signal to noise ratio (SNR) of the measured

true counts are: time of acquisition, randoms and scatter. The SNR of the measured trues changes depending on the number of random and scattered coincidences included in the total counts. The image noise can be quantified from counts recorded in emission scanning, by taking into account the randoms and scatter in the data. Noise equivalent counts (NEC) have been defined by Strother (1990) as:

$$NEC = T / (1 + R/T + S/T) \quad (23)$$

where: T = True coincidences
R/T = Randoms Fraction
S/T = Scatter Fraction

Noise equivalent counts are the reduced number of true counts required to give the same SNR as the measured trues, but without any randoms or scatter contributions. It assumes that the randoms and scatter fractions are known precisely. If there is significant measurement noise in either of these two parameters, then the NEC will be even smaller than that given in eq.(23) (Strother 1990). From this equation it is seen that a higher true count rate and lower randoms (R) and scattered (S) count rates increase the SNR of the scan. This provides a means of comparing the quality of counts obtained with different source strengths and geometry, and with any positron emission tomograph.

Smoothing

A standard smoothing technique is often applied to increase the SNR of acquired scans. Statistical noise is principally high frequency, while the image signal

is principally lower frequency. Therefore by applying a low-pass filter to the sinogram data, the noise is attenuated more than the signal and the SNR of the reconstructed images increases. There is some loss of signal resulting in decreased resolution, however, the noise attenuation is often worth this sacrifice (Dahlbom 1987). Smoothing is especially effective in chest imaging since the signal is severely attenuated through the torso and arms.

Systematic Corrections

Several factors which prevent the measurement on an absolute scale are physical processes which are known to follow specific models. These can be used to correct the data in a systematic and accurate way. Such effects include decay of the isotope during the course of the study, detector dead time, as well as attenuation.

Isotope Decay

Radioactive decay follows the relation:

$$C(t) = C(0) \cdot e^{-(0.693/T_{1/2}) \cdot t} \qquad (24)$$

where:
- $C(0)$ = initial concentration
- t = elapsed time
- $T_{1/2}$ = isotope half-life

If successive counts are recorded over time, then the time course of radioactivity

can be observed in a certain tomographic region. It is often necessary to correct these counts back to the level of C(0). This allows a physiological process such as tracer clearance from a particular organ to be observed independent of the isotope decay. In this case the only parameters required are the half-life of the isotope and the elapsed times (t).

Dead Time

Dead time can be accurately modelled such that the measured counts can be precisely corrected. The correction produces a count rate response of true coincidences versus source strength, which is linear over a wide range of activities. At high count rates this correction can be subject to excessive statistical variations. It is generally desirable to have dead time corrections below a factor of 2.0 in order to have satisfactory results (Knoll 1989). At high count rates, pulse pile-up is not typically corrected, and will result in some random errors in the recorded coincidences.

Attenuation

Currently, a major barrier which complicates the reconstruction of quantitative images is attenuation of the photons as they pass through the surrounding tissue. Photons which are absorbed or scattered in tissue and which do not reach a pair of detectors reduce the total number of coincidences recorded. Those which originate

from the centre of the object have a much lower probability of reaching a pair of detectors than those near the edge. This causes structures which are centrally located to appear with a lower isotope concentration than those near the edge of the object.

Photon transmission can be measured and used to correct the emission data before reconstruction of the isotope distribution. This measurement is performed by placing an external source of radioactivity directly in front of the detectors and measuring attenuation of the flux of photons as they pass through the object to the opposing detectors. The total attenuation of the beam along a given LOR is identical to the attenuation which occurs when the source of activity is within the same object as in Figure 2. This occurs because the photons must travel through the same path length before reaching the detectors regardless of the source position (Webb 1988), i.e.

$$I = I_o \epsilon^{-\mu L} e^{-\mu(T-L)} = I_o \epsilon^{-\mu T} \quad (25)$$

where: T = total absorber thickness [cm]
L = position of source within the object [cm]
μ = attenuation coefficient [cm^{-1}]
I_o = initial beam intensity

Therefore the attenuation correction factors (ACFs) are equal to $e^{\mu T} = I_o/I$. I_o is measured by scanning with no object in the field of view (blank). The attenuated beam I, is then measured by scanning with the object in the field of view (transmission). The ACFs are simply then the ratio of blank/transmission scans. The

corrected emission scan equals:

$$\text{Corrected} = \text{Emission} \cdot \text{Blank/Transmission} \tag{26}$$

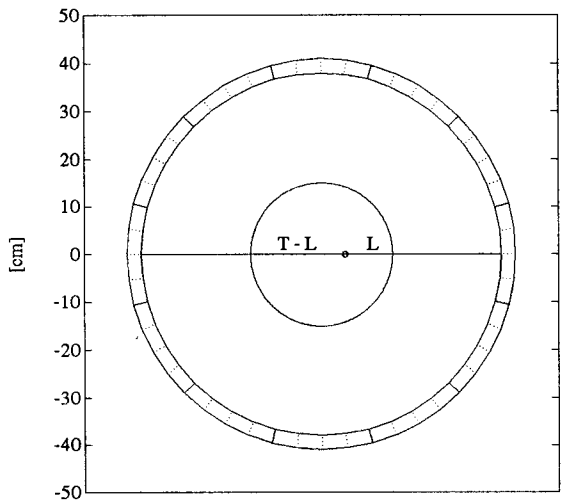

Figure 2 - Attenuation along a given LOR is independent of the source position.

Transmission Scan Quality

Statistical noise is the dominant factor which affects the quality of the transmission scans. It results from randoms and scatter in the measured data, as well as Poisson noise. The acquisition time affects the noise in the scans, as well as object size and density.

Acquisition Time

There are several factors which affect the quality of the measured ACFs. The transmission and blank scans suffer from the effects of counting statistics as well as random and scattered coincidences, as in the emission scans. The longer the accumulation, the lower the noise will be. In general, the blank scan quality is much higher than the transmission scan because of the higher count rate. For acquisitions of equal duration, the statistical noise in the blank scan can be neglected compared to the transmission scan (Dahlbom 1987).

Object Size

More noise is added to a corrected emission scan of a large object than to a smaller object. This is due to the lower count rates obtained in the transmission scan and it results in larger and noisier ACFs in LORs which span a larger object thickness. A typical correction factor is approximately 5 at the centre of the brain, and may be as high as 50 or 100 in studies of the chest. Subsequently, the corrected images are noisier in the centre of the objects than at the edges. The relative noise in a corrected emission scan of a uniform cylinder increases by a factor of $D\mu$, where D is the cylinder diameter (Dahlbom 1987). Smoothing of the blank and transmission scans is often used to reduce the noise at the expense of some spatial resolution.

Transmission Sources

In many scanners, the external source used to measure transmission is a continuous ring containing a positron emitting isotope. This ring can be moved into and out of the field of view as required for the blank or transmission measurement to be obtained. Since there is activity close to all detectors simultaneously, there is a high probability for random coincidences compared to emission scans.

In some cases a point source close to the detectors is used, instead of a continuous ring of activity. This point source is then rotated around the field of view, while the data is being acquired. This is advantageous because a much lower randoms rate results when using this configuration (Carroll 1983). A lower randoms rate produces an image with lower noise, as seen by using the NEC in eq.(23). The diameter of orbit of the point source affects the SNR of the transmission images as well (Yamamoto 1989). It was found that the smaller the orbit diameter, the better the image quality.

In multiplanar systems a rod source oriented axially at the edge of the FOV is used instead of a single point source. The rod source enables additional rejection of scattered and random events, by allowing only coincidence events which pass through the source location to be recorded (Cahoon 1986). In this way coincidences that do not occur on an LOR which intersects with the rod source at any instant in time, are rejected. The rod source is then rotated around the FOV to scan at all angles. This process is referred to as sinogram windowing and can remove up to 95% of the

scattered and random coincidences depending on the width of the window.

Scatter

Scattered coincidences in emission scans increase with the size of the object being imaged. This effect produces a higher count rate than would be expected and subsequent overestimation of isotope concentration by up to 30% (Michel 1989). In transmission measurements, however, this causes an underestimation of the attenuation factor, and a subsequent underestimation in the corrected emission scans. Therefore, the scatter in the transmission scans can actually compensate somewhat for the scatter in the emission scans. In brain studies, the scatter distributions are similar in transmission and emission scans, however, this is not true in general (Michel 1989). Therefore if the transmission scans have been windowed to reduce the scatter or if the ACFs have been analytically calculated, then the scatter must be compensated for separately in the emission data.

Attenuation Correction Methods

There are many methods available to correct for attenuation in tomographic emission scans. These generally trade off accuracy and precision with complexity. The more sophisticated methods have many underlying assumptions which are never valid for all scanning protocols. Scatter in transmission and emission data is a

confounding effect which also makes the corrections more complicated. Therefore it is always necessary to understand the imaging conditions at hand, when evaluating the accuracy of an attenuation corrected emission image.

Calculated Correction

There are two popular methods of performing attenuation correction. The first and simplest method is to use calculated correction factors. This is valid however, only for simple geometries such as circles or ellipses with uniform attenuation within the object. It can be applied with some success, for example, to emission scans of the brain. Transaxial sections of the head are nearly elliptical, and the brain has an attenuation coefficient which is very close to that of water (0.095 [cm^{-1}]). The skull and head holder which have higher attenuation are typically ignored when using this procedure. This can easily result in an underestimation in absolute concentration on the order of 10% (Michel 1989). This method can be time consuming if separate ellipses must be fit to each transaxial section of the head. It can also be very subjective if the ellipses are fit manually, because the operator has no physical landmarks other than the uncorrected emission image. This is particularly difficult in pathological studies where large left/right or anterior/posterior differences exist.

In studies of the torso there are many different attenuating media, principally soft tissue, bone and internal gases (air). This fact precludes the use of a simple calculated attenuation correction for cases other than brain studies. Calculated

attenuation has the advantage that the ACFs are precise (noiseless), so that no noise is propagated into the corrected emission scan. However, if the object boundaries are not smoothly defined, the calculated ACFs will not be accurate.

Measured Correction

The second method is to measure the attenuation using blank and transmission coincidence scans with an external source of positron emitter (Webb 1988). This is much more flexible because no assumptions are made about the shape or composition of the object being imaged. The ACFs are measured for each LOR independent of the geometry or density of the object. Since the correction is obtained as the ratio of two more scans, there is significant noise in these ACFs. This noise is propagated into the corrected emission scan.

It is assumed that the object position is identical in the transmission and emission scans. This is valid for phantom studies, however, during patient studies motion is inevitable. The patient must often lie for hours on the scanner bed before the entire process of transmission, isotope injection and emission scanning is completed. Any motion of the patient during this interval will cause misalignment of the transmission and emission scans, resulting in artifacts at the tissue borders in the corrected images.

Hybrid Correction

Several techniques are being developed to improve the quality and speed of attenuation correction. One promising method is hybrid measured/calculated correction. In this case, a transmission scan is performed as described above. The boundaries between tissues types are then found, and the image is segmented into tissue classes. If an attenuation coefficient is known for each class, then an attenuation correction can be calculated for each LOR through the object. This calculation is called forward projection. The attenuation coefficients can be assumed to correspond to known tissue types such as soft tissue and bone (Tomitani 1987). They can also be calculated as the average of all pixels with a given tissue type in the image or study (Digby 1989). In this case a shorter transmission scan can be performed which enables suitable segmentation of the transmission images.

A hierarchical segmentation can be performed to isolate the known structural features within the transmission images (Michel 1989). If the boundaries are smooth then the calculated factors will be noiseless, and no additional noise will be added to the emission scans. This method is very sensitive to the correct estimation of the tissue boundaries. In some cases the edges are not sharp due to partial volume averaging. For example, at the top of the head many pixels may be part bone and part brain producing a slowly changing attenuation between bone and brain. Any incorrect positioning of the boundary will cause an over- or underestimation of the attenuation along a given LOR.

Postinjection Transmission Measurement

A technique called sinogram windowing has been proposed to perform the transmission scan after isotope injection and emission scanning have been performed (Carson 1988). Sinogram windowing is used to acquire events from detector pairs which are collinear with a point source position. In this case the windowing reduces the emission counts and the scattered coincidences down to 5% when performing the transmission scan. This fraction of the emission scan data is then subtracted from the postinjection transmission scan to obtain the correct attenuation factors. The advantage of this method is that the patient does not need to remain in the tomograph during the uptake period of the isotope, thereby shortening the total study time.

For studies where scanning starts immediately after injection, there is no advantage of using this method. The disadvantage of this method is that the emission scan represents an average of the concentration of isotope integrated over the total scanning time. If the concentration is changing over time then the emission data can not strictly be subtracted from the transmission scan. Another factor is that the noise of the emission scan is folded into the attenuation factors, and subsequently increases the noise of the corrected emission scans. This method could be used in conjunction with hybrid measured/calculated techniques to reduce the statistical noise but may make the results less accurate.

Simultaneous Transmission and Emission Measurement

A similar approach has been taken to perform simultaneous emission and transmission scans using a masked orbiting transmission source (MOTS) (Thompson 1991). Sinogram windowing is again used to obtain the transmission measurements. Detector pairs which are collinear with the source position are used to collect transmission data. Detector pairs which are nearly collinear with the source are rejected. Those which are far from collinear with the source are used to acquire simultaneous emission data. In this case the rod source is shielded with lead to produce a thin fan beam of photons in the scanning plane. This method reduces the contribution of emission data in the transmission measurement to a negligible amount of 0.5%. It obviously eliminates the need for a separate transmission scan, while sacrificing a decrease in the emission counting efficiency. The technique is only applicable for studies in which the emission scanning time is sufficiently long to acquire a transmission scan as well.

Singles Transmission Measurement

The disadvantage of using a rotating source is that the dead time of the detectors next to the source is higher than when the ring source is used. In order to obtain a comparable count rate to the ring source, all the activity of the ring source must be concentrated in the rod source. This causes the coincidence counting efficiency to decrease, but this is not a major problem because the rod source strength

can be increased to compensate.

Further gains in count rate can be made if the coincidence requirement of transmission measurements is removed. The coincidence efficiency is equal to the product of the singles efficiencies at the two detectors (Derenzo 1975). Counting efficiency is inversely proportional to the dead time losses. When using a rod source, the dead time of the detector near the source is high compared to the opposing detector. This causes coincidence counts to be lost when the near detector is recovering from an event. If the rod source is positioned in front of a given detector and single photons are counted in the corresponding fan beam as in Figure 1, then the counting efficiency increases dramatically. The fan beam LORs are still uniquely defined because the position of the source is known. Coincidence projections can therefore be assembled in this mode given each detector location and the source position.

CHAPTER III

Single Photon Transmission Measurement

Acquisition and Corrections

Singles transmission measurement was implemented on the PET scanner at McMaster University (SIEMENS/CTI ECAT 953, Knoxville TN). Data correction and calibration methods were developed to enable accurate calculation of the measured attenuation correction factors. Experiments were carried out to determine the correction parameters and to evaluate the performance of the technique.

Positron Emission Tomograph

The PET scanner at McMaster University is a state of the art tomograph that performs volumetric imaging. It has a 40 cm wide transaxial field of view, and produces 31 images within the 10.8 cm axial field of view. It uses block detectors of BGO coupled to 4 PMTs. Each block is manufactured to produce a matrix of 8 by 8 detectors. The signals from the 4 PMTs are used to perform position encoding, i.e. to determine in which detector a given photon interacted. Energy encoding is also

done using these signals to separate photopeak events from scattered events. The energy resolution of these detectors is approximately 30%. Therefore, the energy discriminator settings on the ECAT 953 accept events between 250 and 850 [keV].

Four blocks share common electronics in what is called a bucket, and 12 buckets make up one tomographic ring. The ECAT 953 is a two ring machine, with an axial width of 16 detectors, producing 16 straight planes and 15 cross planes between the physical detectors. There are 384 detectors around the circumference giving a total of 6144 detectors. The configuration of buckets, blocks and detectors is shown in Figure 3.

Singles Acquisition

The ECAT 953 is equipped with a rotating source holder with an angle encoder that is capable of positioning to within 0.35 degrees. A rod source was built which mounts onto this holder and consists of a long 9 mm diameter aluminum cylinder. The centre of the cylinder is bored out to hold a 5 mm diameter by 20 cm long glass tube which can be filled with radioactivity. The inner diameter of the tube is 4 mm. This rotates at the edge of the field of view with an orbit diameter of 48.0 ± 0.2 cm.

To perform a singles scan the rod is moved in discrete steps to each of the 384 detector locations around the ring. At each rod location, a 10 s count (histogram) is acquired on the 7 opposing buckets. This is a four step process since each block in

a bucket must be acquired separately due to hardware and software restrictions. Each block reports counts for its 64 detectors, and these are saved in text files. Therefore, with one revolution of the rod source, the block data enables measurement of the 8 axial planes in one bucket ring. In addition to the block data, total singles rates for all four blocks in each bucket are acquired and saved. These rates are measured independently by the hardware and are dead time corrected values.

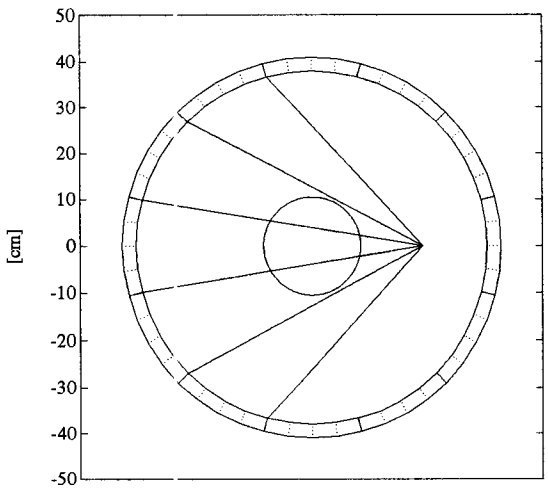

Figure 3a - There are 12 buckets in one ring of the McMaster PET scanner (SIEMENS/CTI ECAT 953).

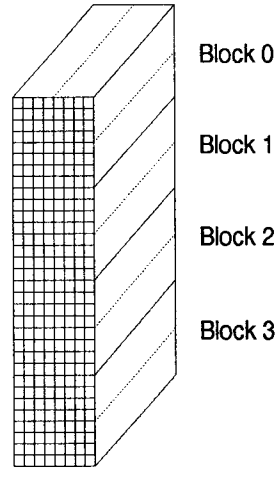

3b - Blocks and detectors in one bucket.

The total counting time is therefore 10 s × 384 detectors = 64 minutes. However, due to the time required to rotate the source in discrete steps and to transfer the block data over a serial line, the total acquisition time is actually 12 hours. (Software is in Appendix A). This poses some logistical problems in acquiring a complete scan because a long lived source of positron emitting isotope is not currently available in this laboratory. ^{18}F is commonly used for experimental purposes, but its

half-life is only 110 minutes. In some cases where all angles must be sampled to acquire a complete scan, ^{64}Cu has been used which has a half-life of 12.8 hours.

Singles to Coincidence Sinograms

In order to create a coincidence sinogram using singles, one fan beam is acquired for each detector location. The lines of response in the sinogram are defined using the rod source position (solid circle) and the opposing detector locations (d2) as shown in Figure 4.

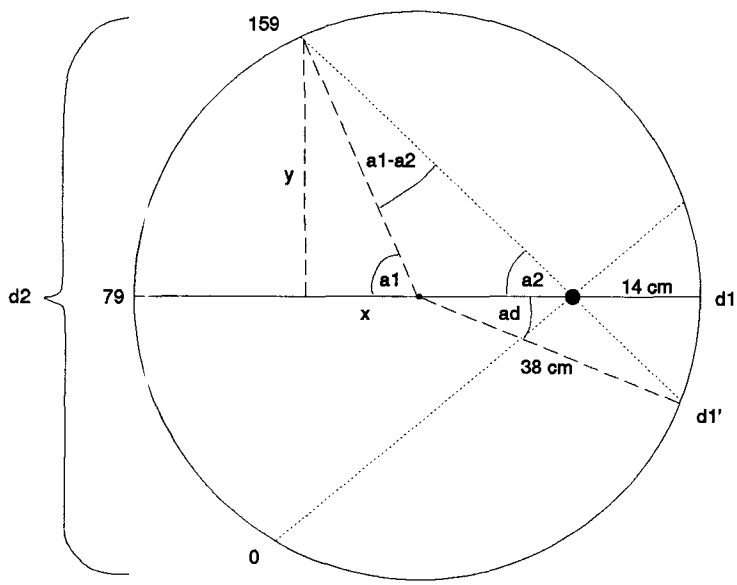

Figure 4 - Spatial resampling geometry. Coincidence sinograms are generated by computing d1' for each d2 detector.

The rod source is a significant distance away from the detectors, therefore the geometry of the singles transmission scanning is not identical to the coincidence transmission method. This produces a magnification of objects in the field of view which must be corrected.

Spatial resampling was implemented to convert the data from source to detector fan geometry. Source detector offsets are calculated for each ray (d2) in the fan beam. The offsets then define new source detector positions (d1') which are used to compute the correct coincidence rays. Linear interpolation is used in the radial direction and nearest neighbour interpolation is used for the angles. The projections are resampled while the sinogram is constructed from the raw data (Software is included in Appendix A). The critical measurements needed for this correction are the detector ring radius (38.0 cm) and the source orbit radius (24.0 cm). Therefore the source orbits at a distance of 14.0 cm from the detector ring. The correction is relatively simple, requiring only a few trigonometric calculations:

$$
\begin{aligned}
&\text{orbit} = 24.0 \\
&\text{radius} = 38.0 \\
&d2 = [0,159] \\
&a1 = 2\pi/384 \cdot (d2-79) \\
&y = \text{radius} \cdot \sin(a1) \\
&x = \text{radius} \cdot \cos(a1) + \text{orbit} \\
&a2 = \text{atan}(y/x) \\
&ad = 2.0 \cdot a2 - a1 \\
&d1' = ad \cdot 384/2\pi
\end{aligned}
\qquad (27)
$$

Three resampled sinograms are shown in Figure 5. Brighter regions correspond to detectors with higher counts in the left and middle sinograms. A transmission

sinogram of a 21 cm water cylinder is shown on the left. The central dark region in the left sinogram is the area attenuated by the cylinder. The resampling has the effect of narrowing the radial axis of the sinogram, creating the black bands on the right and left hand sides. These bands correspond to detectors which are not sampled in the singles geometry. The sharp diagonal artifact is at the interface between the first and the last positions of the rod source. Since the source decays over the course of the acquisition, there are not as many counts at the end (above the diagonal) as there are at the start (below the diagonal) of the scan. Since the blank scan is acquired with the identical timing, the resulting attenuation correction sinogram shown on the right does not have this artifact.

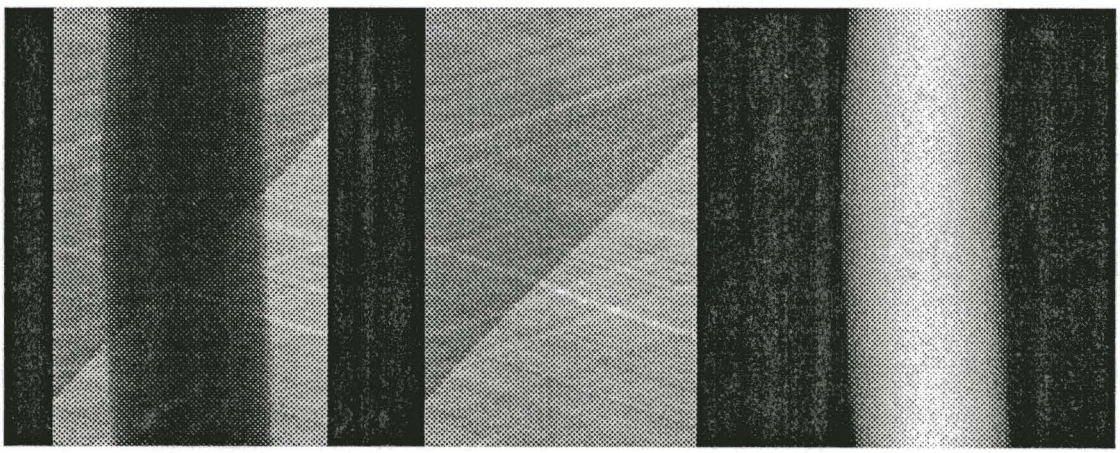

Figure 5 - Sinograms of a 21 cm water cylinder which is centred in the FOV. The transmission (left), blank (middle), and attenuation correction (right) scans are shown.

Efficiency Normalization

In order to obtain quantitative attenuation factors, counts must be normalized for

variations in detector efficiency. Two scans with the rotating rod source are required to calculate the ACFs. The first is a blank scan which is performed with nothing in the field of view. The second is the transmission scan which is done with the object of interest in the field of view. The ACFs are computed as the ratio of the blank/transmission scans, therefore the efficiency correction is included in this process already. The ratio is taken detector by detector, therefore the resultant ACFs are independent of detector efficiency.

Attenuation Image Reconstruction

Images of attenuation coefficient are used to evaluate the quality of the measured attenuation correction data. The images are generated using the blank (I_o) and transmission (I) sinograms. Software supplied with the scanner, calculates the ratio of these two scans, computes the log, and divides the counts by the sampling distance, i.e.

$$\begin{aligned} p(r,\theta) = \quad & \ln(I_o/I) = \mu L \qquad \text{for an object of uniform density} \\ & = \int \mu(x,y)\, dL \text{ for an object of varying density} \\ & = \int \mu(x,y) \cdot dL/ds\, ds \end{aligned} \tag{28}$$

The division by the sampling distance (0.3129) is a change of variables (dL/ds) necessary to obtain the attenuation coefficient in units of [cm^{-1}]. When this log correction sinogram (Figure 5, right) is backprojected into an image, the pixel values are representative of the measured attenuation coefficient, e.g. 0.095 [cm^{-1}] for water.

Block Dead Time Correction

When measuring the attenuation factors, if the count rates are not dead time corrected then the values obtained are too low. The blank scan has higher dead time losses (lower efficiency) than the transmission scan, therefore the uncorrected ratio of blank/transmission is too low. A dead time correction was developed to enable measurement of quantitative attenuation factors.

In block type systems, the detectors in a block share common components, such that when an event is detected in any one detector, the entire block is unable to count another event during the dead time interval. The average dead time corrected bucket singles rate is also measured independently by the hardware, and saved by the singles scanning software. The detectors in a given bucket can be corrected as a whole using the bucket singles rate. However, the blocks within a bucket may have different dead time losses, therefore an additional block correction must be made within each bucket. Without the additional block correction, sharp discontinuities are produced at the block interfaces.

The total block count rate response was found to follow a nonparalyzable dead time model as given in eq.(11). In order to perform the block correction, fan beam profiles are acquired with the source positioned at a given detector location as shown in Figure 3. In each of the 8 tomographic planes a profile (with 160 detectors) is computed from five buckets of data (256 detectors each). Within each bucket, the four blocks are corrected using eq.(29). The factor n/m is the nonparalyzable block dead

time correction in eq.(11). The factor b/c ensures that the sum of the four dead time corrected block totals equals the independently measured bucket total. The only unknown parameter is the block dead time (τ) in eq.(11), which is estimated experimentally. The correction is summarized below:

MD_{64} - Measure Detector profiles from 4 blocks. (There are 64 detectors per block.)

m - Sum within each block. (4 Measured block totals)

n - Correct block totals with eq.(11).

c - Sum 4 blocks. (Corrected bucket total rate.)

b - Measure bucket total singles rates. (Dead time corrected independent measurement.)

CD_{64} - Correct Detectors with:

$$CD_{64} = MD_{64} \cdot (n/m) \cdot (b/c) \qquad [cps] \qquad (29)$$

The components of the dead time correction are shown in Figure 6. A sample profile of attenuation correction factors (ACF) in one plane is shown in Figure 6a. This profile was obtained by taking the ratio of the raw blank/transmission scans of a 21 cm water phantom. There was 5 mCi of activity in the rod source, and no dead time correction was applied. The severe fluctuations observed are at the block interfaces, while within a block the response is smooth. The maximum ACF in this profile is approximately 1.5. The maximum ACF through the middle of a 21 cm water phantom should be 7.4.

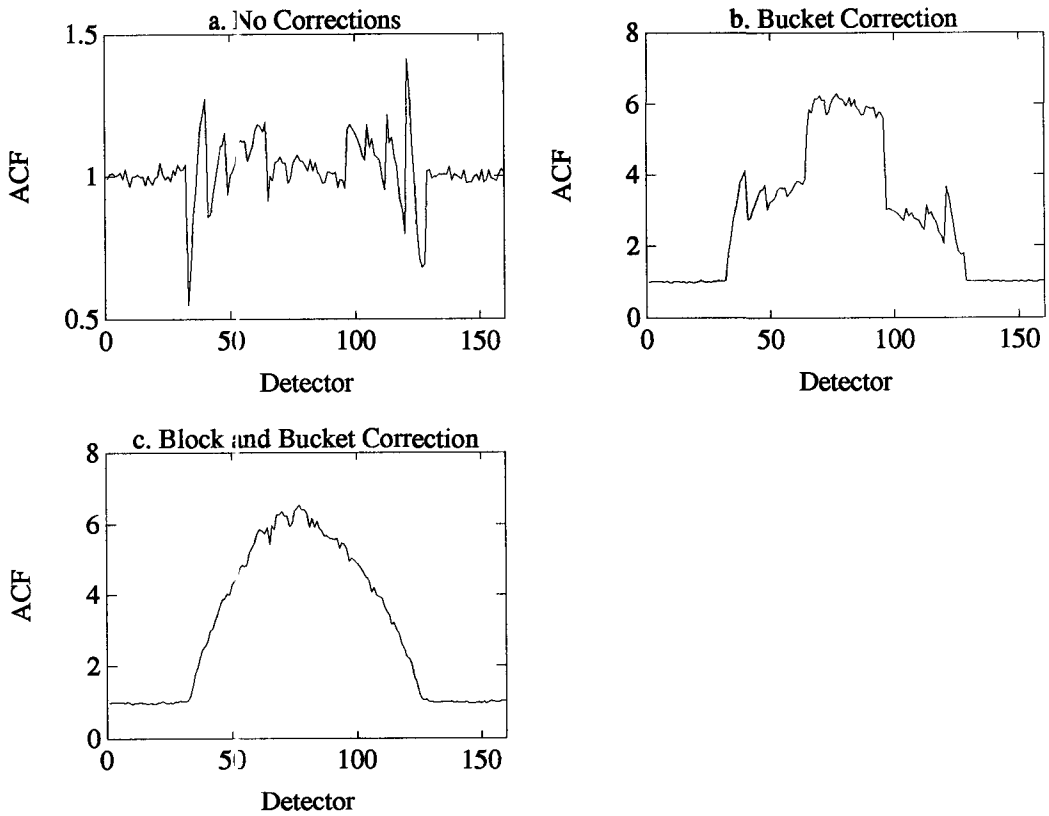

Figure 6 - Attenuation Correction Factor (ACF) profiles of a 21 cm water cylinder, obtained with various dead time corrections.

The effect of the bucket correction is demonstrated in Figure 6b. This is the bucket corrected version of Figure 6a. The two outside buckets do not record any attenuation, and produce ACF values of unity. Three distinct buckets can be identified which do span the attenuated fan beam across the phantom as shown in Figure 3. They correspond to the three plateaus of ACFs which are greater than unity. Within a given bucket, the blocks which project close to the edge of the phantom have a much higher dead time than the blocks closer to the centre of the phantom because of the different count rates. The three discrete levels are due to the fact that the bucket

singles rate is not applicable to all four blocks in the bucket. These rates are dead time corrected, but represent the average of the four blocks. The middle bucket has been corrected close to the appropriate level with a maximum ACF of 6.2. The low value is due to the nonlinear bucket response and the acceptance of scattered events.

The response within a block is smooth and of the proper orientation. The nonparalyzable model is used to correct the block responses up to the measured bucket rates. For a block sum count rate the dead time used is 0.175 ms. If this block dead time correction is applied within each bucket, a smooth ACF profile is obtained. This profile is shown in Figure 6c, and is again the corrected version of the data shown in Figure 6a. There are still some discontinuities, however, these are due to the statistical variations in projections through the centre of the phantom where the count rate is lower.

Performance Experiments

Several objects have been scanned to verify the accuracy and precision of the method. Many of the performance tests were described previously in Chapter II. Some are used to determine more than one aspect of the performance, and so, are described here before the results are presented. Experiments performed during the development of the technique are not discussed further.

In most cases only one profile from a given angle was obtained and compared

to a calculated profile. In other cases images were reconstructed by sampling at all angles. A complete scan takes 12 hours so ^{64}Cu was used for some experiments. When ^{18}F was used to do a complete scan, only every second source position was acquired. This reduced the scan time by a factor of two. It could therefore be completed with the source decaying for approximately 3 half-lives. There may be a slight reduction in image resolution in this case.

Decaying Source Profiles

A count rate experiment was done with a decaying source of ^{13}N, which has a half-life of 10 minutes. The source was collimated with 3 cm by 3 cm tapered tungsten septa. The septa thickness was 1 mm next to the source and 3 mm at the beam exit point. The centre to centre spacing was 0.675 cm which is equivalent to the detector spacing. The source was positioned 4 cm away from the septa. 8.0 mCi was loaded into the rod source at the start of the experiment.

Profiles were acquired of blank and transmission measurements at 5 minute intervals. The counting time was 10 s per block. A total of 14 blank and transmission measurements were made over a period of 70 minutes (7 half-lives). The dead time corrected bucket rates were also measured to determine the response to source strength.

Water Cylinder Profiles

Profiles were obtained through water-filled cylinders of various sizes. A small extent source was used to reduce acceptance of events from adjacent planes. 0.5 mCi of ^{18}F was used in a syringe with 0.8 cm diameter and 1 cm length. Several 100 s blank profiles were acquired. 100 s transmission profiles were measured through 5 cm, 12 cm, 21 cm and 30 cm diameter cylinders.

Edge Response Profiles

Several source configurations were used to examine the edge response of a 21 cm cylindrical phantom. The point source described above was positioned as shown in Figure 7 with respect to the phantom edge. Profiles were then obtained in the eight planes of one ring. Two other tests were performed with a longer rod source. Eight profiles were first measured with a 20 cm long rod source. Next, a 5 cm rod source was collimated with the septa described above, and used to obtain the eight profiles.

Centered Phantom Images

A complete scan of a 21 cm diameter by 30 cm water-filled cylinder was acquired as shown in Figure 3. The rod source was filled with 13.7 mCi of ^{64}Cu and used to acquire the transmission scan. This is approximately equal to 2.6 mCi of ^{18}F

or ^{13}N because the branching ratio of ^{64}Cu is 19%. The scan was acquired with a 10 s count at each detector and no source collimation was used.

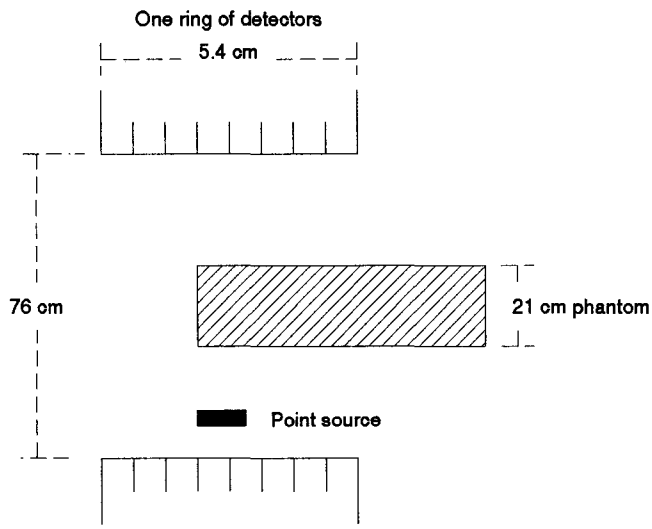

Figure 7 - Edge response experiment. The axial extent of the point source is 1 cm.

Off-centre Phantom Images

A complete transmission scan of a 12 cm diameter by 30 cm water cylinder was also performed as shown in Figure 8. One edge of the phantom was positioned at the centre of the FOV. In this case the rod source was filled with 5.0 mCi of ^{64}Cu. This is approximately equivalent to 1.0 mCi of ^{18}F. The blank scan measurements were made with the identical source about 12 hours earlier. All scans were acquired with 10 s counts at each detector and no source collimation was used.

Object Density Images

Images of a 21 cm diameter water phantom with a 2 cm cylindrical air insert and a 2 cm aluminum insert were also acquired. These tests were done with 400 uCi of ^{18}F in a 4 mm diameter syringe with approximately 2 cm length. Every second source position was used in this case to rotate around the FOV before the source strength decreased unacceptably. The total time required was 5.5 hours, therefore the source had decayed to about 50 uCi at the end of the experiment.

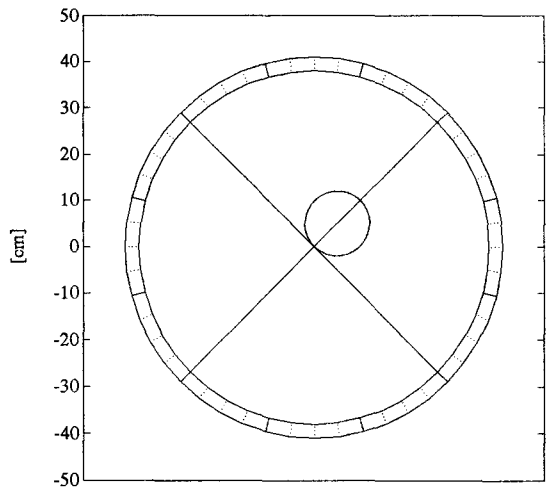

Figure 8 - 12.0 cm off-centre water phantom geometry.
One edge is centred in the FOV.

Energy Spectra

The energy spectra of the ring and rod sources were measured in 10 keV increments. The 21 cm phantom was placed in the centre of the FOV and the bucket singles rates were used to obtain the response at each energy level. The rod source was loaded with 0.5 mCi of ^{18}F, and the procedure was performed without any source collimation. The process was repeated with ring source which currently contains approximately 0.5 mCi of ^{68}Ge in each of 16 rings.

Calculated Profiles

Software provided with the tomograph was used to calculate the profiles of water-filled cylinders of various diameter. These calculations were done with the object centred in the FOV and no scatter component included. The attenuation factors were simply determined by the chord length of a given ray through the cylinder, and the linear attenuation coefficient of water (0.095 [cm^{-1}]).

Simulated images were also reconstructed using calculated profiles of the 21 cm phantom. The noise in these images was still around 0.5%. This is the minimum noise which can be achieved using the SIEMENS/CTI PET reconstruction process.

Coincidence Experiments

Several transmission experiments were performed in coincidence mode using the ring and rod sources. These scans were all 64 minute acquisitions. This is equal to the total scanning time of the singles method, i.e. 384 detectors · 10 s/detector = 64 minutes.

The first of these is a rod source transmission scan of the 21 cm phantom, with a mean activity of 2.0 mCi of ^{18}F. This scan was then repeated using the ring transmission source. The density phantom was also scanned with the ring source to compare with the singles transmission images.

Performance Results

The system dead time is estimated, and then an analysis of the performance experiments is carried out to quantify the results. The results include measures of accuracy, precision, and resolution of the singles transmission measurement technique.

Dead Time Correction

The nonparalyzable dead time correction requires that the block dead time (τ) be determined accurately. This was performed using the decaying source experiment

data shown below in Figure 9. The 21 cm cylinder curves were measured in a block through the centre of the phantom. The blank curves were taken using the same block and bucket but with the phantom removed.

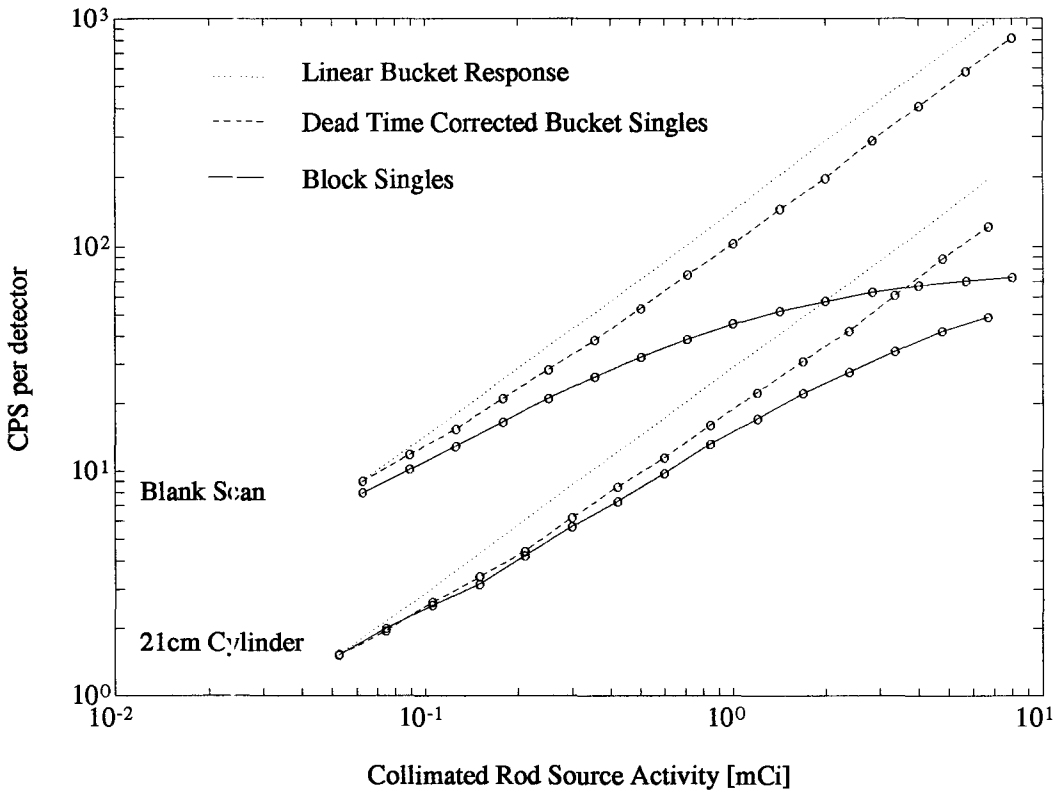

Figure 9 - Block and Bucket singles count rate response of a collimated rod source.

The nonparalyzable dead time correction formula is given as $n = m / (1 - m\tau)$. One can also measure the bucket dead time corrected singles rate (b). The block rate will be a constant fraction of the bucket rate for a given geometry, i.e. $n = kb$.

If n is equated in these two formulas we obtain an equation relating the measured block count rate (m) to the fraction of the bucket rate incident on the block (m/b).

$$m/b = k - k\tau m \qquad (30)$$

This equation should yield a straight line if the dead time model is valid at all count rates. Therefore by fitting a line through these points the intercept (k) is determined, and then the dead time is simply the negative slope of the line divided by the intercept.

A typical fit of the 21 cm phantom data in Figure 9, is shown in Figure 10. The curve is linear over a wide range of counts. This indicates that the model can be used to correct the measured block rates to the measured (dead time corrected) bucket rates. The estimate of the dead time from the slope and intercept of such lines is 0.178 ± 0.008 ms. The error estimate was determined from the standard deviation of blocks measured in one bucket through the centre of the 21 cm water phantom (see Appendix B).

The dead time estimate obtained from blocks in different buckets is 0.174 ± 0.019 ms. This is a considerable range and seems to indicate a wide variation in the block count rate response. However, as illustrated later, this range does not have a large effect on the quality of the ACF data, because the bucket singles rates used in the correction are more stable. This dead time correction allows suitable profiles to be acquired over a range of activities from 0.1 mCi to 10 mCi.

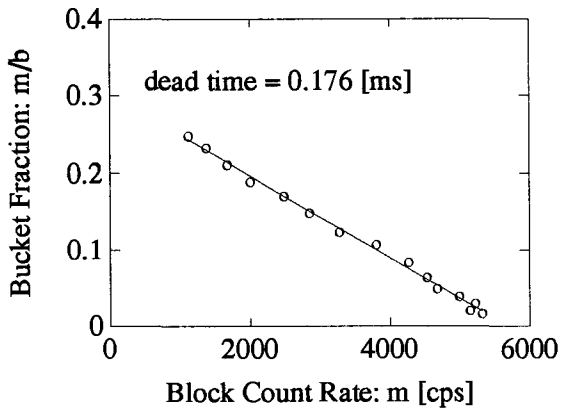

Figure 10 - Typical dead time estimation curve of block count rate versus bucket fraction.

The bucket count rate response is shown in Figure 9 as well. Although the measured bucket rates are nearly linear with activity in the source, there is a slight overestimation at low count rates relative to the higher count rates. This results in an underestimation of the ACFs in regions with high attenuation.

Low ACF values may be associated with acceptance of scattered photons. However, the block dead time has a strong effect on the apparent scatter properties in a reconstructed attenuation coefficient image as well. The dead time correction is most important in buckets which project through the edge of the phantom, or through any other large change in object density. The dead time value determines how the four measured block counts are distributed within a given bucket. If the dead time correction is too high, the effect is to increase the apparent scatter in the ACF data. If the dead time is too low the result is to lower the apparent scatter. These effects

are illustrated in Figure 11. These are smoothed attenuation coefficient images of a 21 cm water phantom, corrected with block dead time values of τ = 0.135, 0.175, and 0.215 ms. An attenuation coefficient image with high scatter in the transmission data will have a lower attenuation coefficient in the middle of the phantom (right). Low scatter in the transmission (and blank) data will result in a uniform image (middle). The image with higher attenuation coefficient in the centre is not physically possible (left).

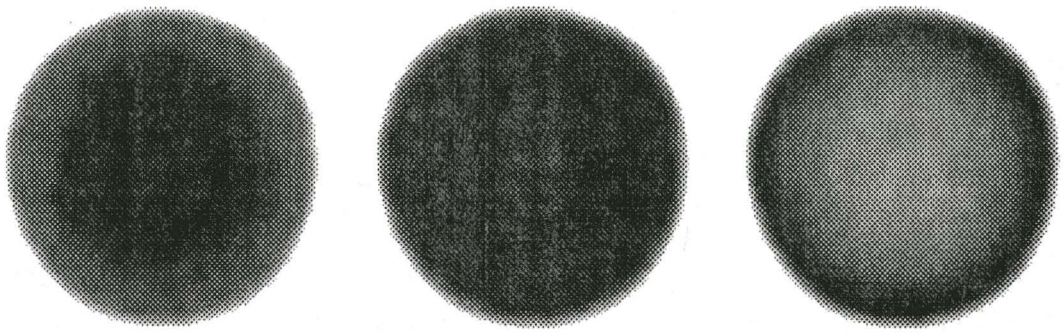

Figure 11 - 21 cm water phantom images reconstructed with block dead time values of 0.135 ms (left), 0.175 ms (middle) and 0.195 ms (right).

If we assume that there is very little scatter in this transmission data, the uniformity of the centre image in Figure 11 would lead us to believe that a dead time value of τ = 0.175 ms is an appropriate value for a 21 cm water phantom (which is similar to typical brain imaging). This value also appears constant for all blocks and buckets since the angular uniformity is good as well. Current coincidence transmission images obtained with the ring source show no apparent scatter, as in the centre image of Figure 11.

We have observed that the bucket singles rates of the uncollimated 20 cm rod source are approximately 1.4 times that of the 5 cm collimated source shown in Figure 9. A point source produces approximately twice the count rate of the collimated rod source with the same total activity. These count rates are shown in Table 3.

TABLE 3

DEAD TIME CORRECTED SINGLES RATES MEASURED WITH VARIOUS ROD SOURCE CONFIGURATIONS AND NO ATTENUATION.

Source Type (0.5 mCi)	Detector Singles Rate [cps]
5 cm Collimated Rod Source	50
20 cm Uncollimated Rod Source	70
2 cm Point Source	110

Uniformity

The uniformity was evaluated using the 21 cm water phantom images shown in Figure 12. In order to scan at all angles ^{64}Cu was used to complete the acquisition with reasonable activity in the rod source. 19% of the decays of ^{64}Cu result is the emission of a positron. In 0.5% of the cases the decay is electron capture to an excited state of ^{64}Ni, which subsequently emits a 1.34 MeV photon. If these higher energy photons are scattered in the detector, slightly more 511 keV photons may be counted. If there are more counts in the transmission scan, then the resulting ACFs

will be too low, and the absolute μ values may be inaccurate.

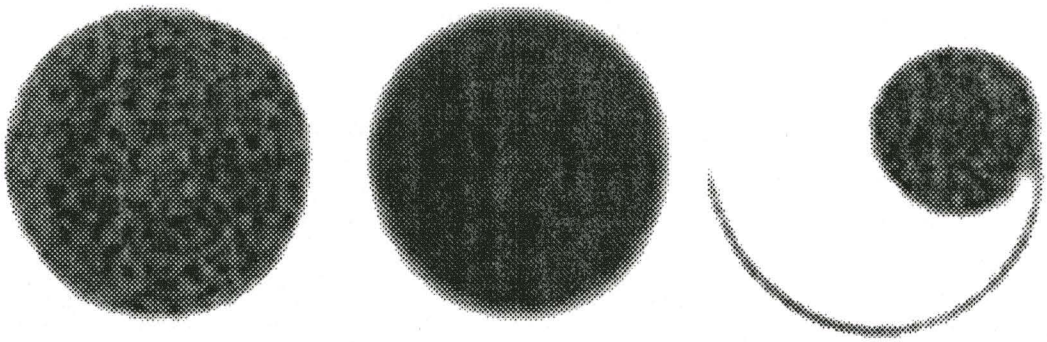

Figure 12 - 21 cm uniform phantom images without smoothing (left) and with 11 mm Gaussian smoothing (middle). 12 cm off-centre phantom without smoothing (right).

Several regions were drawn and the percent noise was calculated for each. These results are summarized in Table 4. The noise level was 3.14 ± 0.36% in the unsmoothed image. There are some subtle ringing artifacts due to the linear and nearest neighbour interpolation used when resampling the sinogram. If the blank and transmission scans are smoothed with an 11 mm Gaussian filter before calculating the ACFs then the image noise decreases to 1.34 ± 0.36% in the identical regions. The attenuation coefficient inside these regions is 0.076 ± 0.001 [cm^{-1}]. The low value is due to the nonlinear bucket response and the acceptance of scattered photons since an uncollimated rod source was used. The average attenuation coefficient of the 12 cm phantom is 0.078 [cm^{-1}].

The uniformity was also examined in the 21 cm density images shown in Figure

13, in regions with only water. The noise in these regions was 2.38 ± 0.83% with smoothing. In these images the μ values obtained with ^{18}F and half the scan angles was 0.084 [cm^{-1}]. This is closer to the true linear attenuation coefficient of water (0.095 [cm^{-1}]). The higher value obtained with the ^{18}F is either due to the absence of the high energy photons of ^{64}Cu or to the smaller extent of the source used in this experiment. Since the proportion of 1.34 MeV photons is small, the difference must be due to the small source size which produces less cross-plane scatter than the 20 cm rod source.

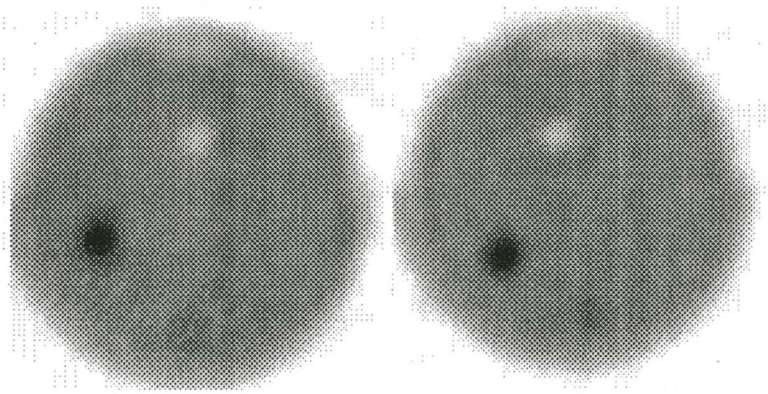

Figure 13 - Images of a 21 cm water phantom with 2 cm aluminum and air inserts. On the left is a singles transmission image obtained using a 0.5 mCi point source. On the right is a ring source coincidence transmission image.

TABLE 4

ACCURACY* AND PRECISION IN ATTENUATION COEFFICIENT IMAGES MEASURED WITH SINGLES TRANSMISSION.

Transmission Source	Cylinder Diameter [cm]	μ_{water} [cm^{-1}]	Noise (σ/m) [%]
20 cm Rod	21	0.076	3.14
20 cm Rod	21 (smoothed)	0.076	1.34
20 cm Rod	12	0.078	3.18
2 cm Point	21 (smoothed)	0.084	2.38

*μ_{water} at 511 keV is 0.095 [cm^{-1}]

Object Size

The correct object diameters were obtained when 5 cm, 12 cm and 21 cm cylinders were scanned. The object size is determined by examining the width at the base of the curve, which corresponds to the edge of the object being scanned. The measured singles profiles and calculated profiles are shown in Figure 14. The measured profiles have been spatially resampled, which is why the ACFs are zero at the edges of the FOV. These coincidence LORs have not been sampled in the singles geometry. This verifies that the spatial resampling is accurate for objects up to 21 cm in diameter centred in the tomograph. Since this resampling is a closed form expression, the correction is likely accurate over the entire FOV. The base width is different in the 30 cm phantom because it was 4 cm off-centre in the FOV. The two

peaks on either side of the 12 cm profile are caused by the head holder.

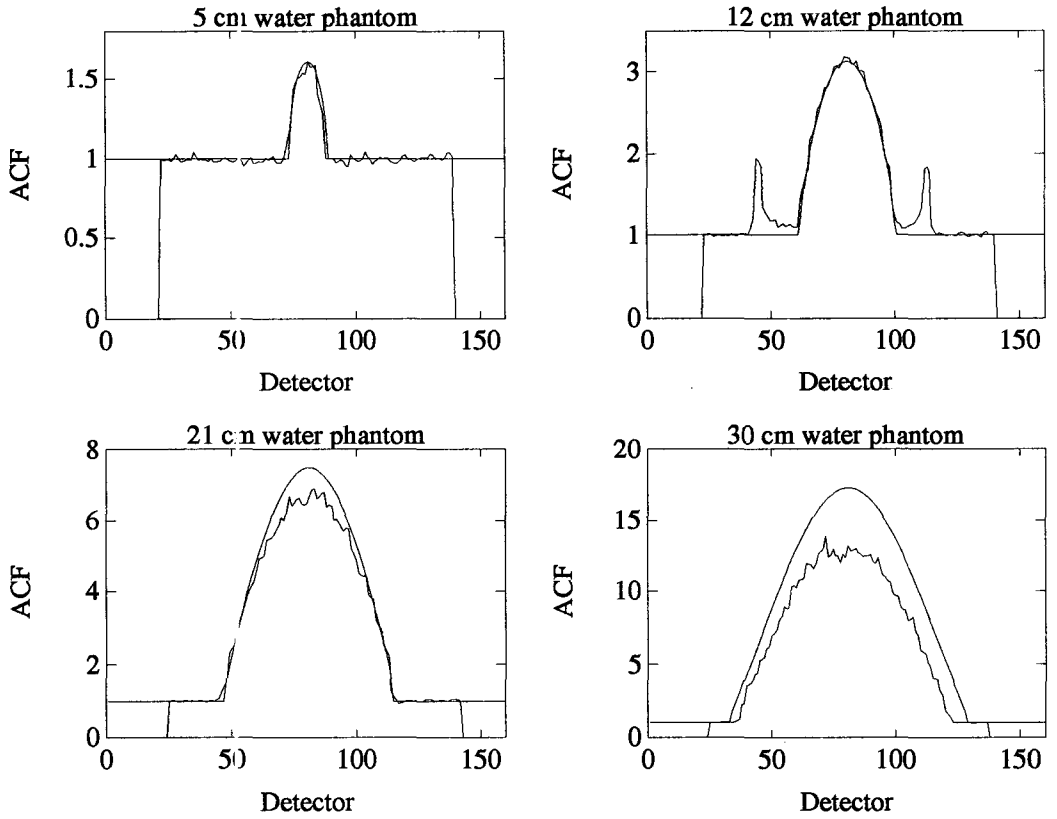

Figure 14 - Profiles of water cylinders of various sizes. The smooth lines are calculated profiles. The measured profiles are noisy, and have some unsampled detectors where the ACFs equal zero.

N.B. 14b is taken with the headrest; 14a,c,d are without the headrest.
14d is not centred in the FOV.

The correct diameter is also obtained in the 21 cm water images in Figure 12, by measuring the FWHM through the centre of the phantom. The resampling is also verified by examining the 12 cm off-centre phantom image. The fact that this scan produced a circular image with the correct diameter means that the resampling is correct. If it had not been accurate the phantom would have appeared magnified toward the edge of the FOV.

Object Density

Using the density images shown in Figure 13, the attenuation coefficients of aluminum and air were compared to water, to determine the response of the ACFs to different density materials. The results are shown in Table 5; μ_s is obtained with singles transmission measurement, and μ_c is obtained with coincidence transmission measurement. The attenuation coefficient of aluminum is 0.226 at 511 keV (Johns 1971). This is the maximum attenuation coefficient encountered in normal transmission scanning. The ratio of the attenuation coefficient of aluminum to water is within 2.5% compared with coincidence transmission scanning. The ratios of air to water are within 15%. The larger variation here may be due to the fact that only half the scan angles were used.

TABLE 5

MEASURED ATTENUATION COEFFICIENTS

Object	Singles Transmission μ_s	μ_s/μ_s^{water}	Coincidence Transmission μ_c	μ_c/μ_c^{water}
Water	0.084	1.0	0.093	1.0
Aluminum	0.166	1.98	0.189	2.03
Air	0.039	0.46	0.037	0.40

The ACFs were also checked using the profiles shown in Figure 14. The 5 cm and 12 cm cylinders were very close to the calculated curves. A 21 cm and 30 cm

cylinder showed ACF underestimation of 10% and 20% respectively, due to the inaccurate dead time correction or scatter. The 30 cm phantom was not quite full of water which may account for up to 15% of the difference.

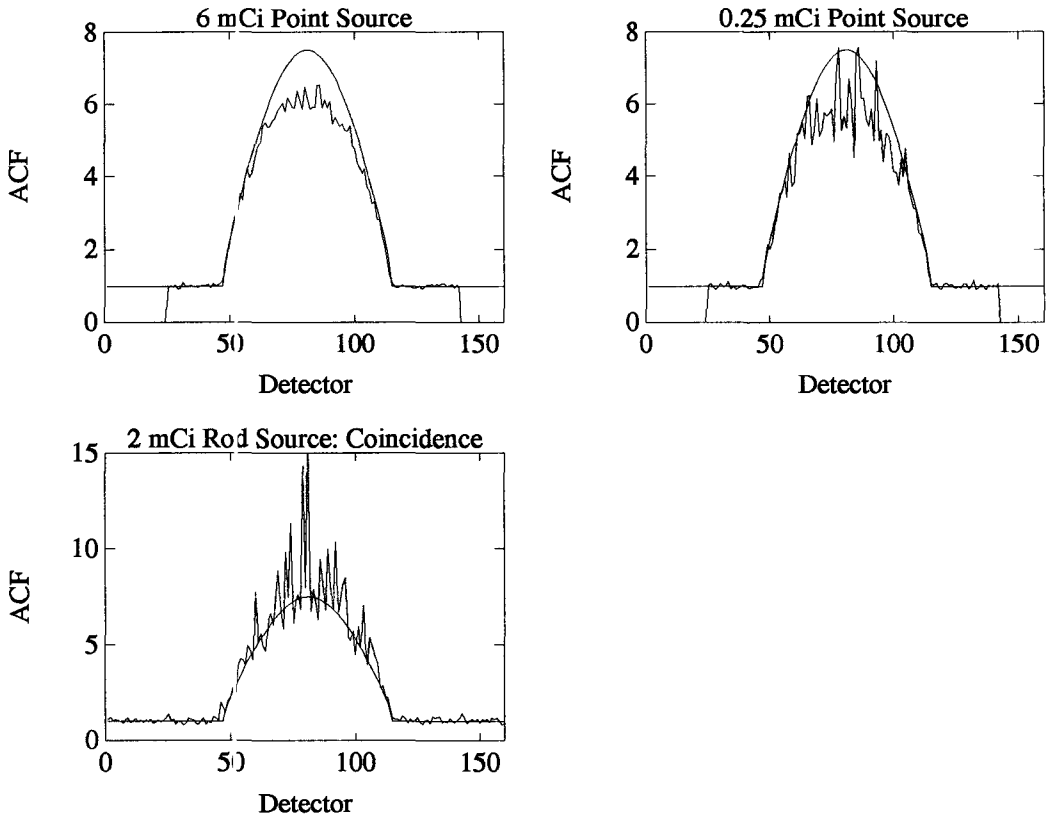

Figure 15 - 21 cm water cylinder profiles obtained with point sources and singles acquisitions. The rod source profile was obtained in coincidence mode. The smooth curves are the calculated profiles.

Singles profiles at two activity levels are shown in Figure 15, as well as a coincidence profile measured with the rod source. Total acquisition times are equivalent in all cases. The maximum ACF values are roughly equal in the two

singles profiles, which indicates that the singles transmission measurement is independent of source strength. Even with only 0.25 mCi in the point source, the data quality is significantly better than that obtained in coincidence mode with a 2 mCi rod source.

Transaxial Resolution

Transaxial resolution was measured using the image of the 12 cm water cylinder off-center in the FOV (Figure 12). Resolution was estimated by measuring the half width at half maximum (HWHM) at the edge of the phantom at various angles from the centre of the phantom. The distance from the centre of the FOV was calculated for each angle and the FWHM calculated as 2·HWHM. The results are shown in Figure 16. The resolution is 5 mm at the centre of the FOV and increases to a maximum of 8 mm at 12 cm from the centre. The true resolution is likely better than shown between 8 cm and 11.5 cm because the FWHM decreases markedly at 12 cm. These values are worst-case estimates since there is still some image noise at the edge of the phantom. Ideally, a longer acquisition would be used to obtain measurements which are practically free of statistical noise. These results are comparable to those measured using emission images during the tomograph acceptance tests. In fact an 11 mm Gaussian smoothing filter is typically applied to the blank and transmission data before computing the ACFs, therefore even 8 mm resolution is quite acceptable.

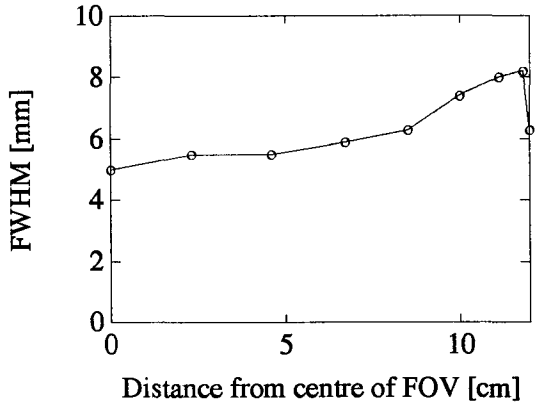

Figure 16 - Transaxial resolution measured at the edges of the 12 cm off-centre water cylinder shown in Figure 12.

Axial Resolution

Axial resolution was measured using three source configurations, and the results are illustrated in Figure 17. Eight axial profiles of measured attenuation correction factors (ACF) are shown. The spacing between profiles is 0.675 cm, and the total axial FOV is therefore 5.4 cm. The HWHM was estimated from these profiles and multiplied by two to get FWHM values. A 20 cm line source was used first which spanned the axial FOV of 10.8 cm. The FWHM of this method is approximately 4 cm, which is unacceptably large. Next the source was collimated with the 3 cm by 3 cm tungsten septa described earlier. This resulted in a FWHM of 2.5 cm and indicated that a collimated line source may be practical for singles attenuation scanning. Finally, a point source was placed at the leading edge of the 21 cm water cylinder as shown in Figure 7, and produced a FWHM of 1.5 cm. The point source response is

a mixture of the intrinsic axial resolution and the width of the source itself. The source width causes some blurring of the intrinsic response because different lengths of the phantom are traversed from different points within the source. In fact this is true for the rod source configurations as well. The blurring effect is reduced with collimation.

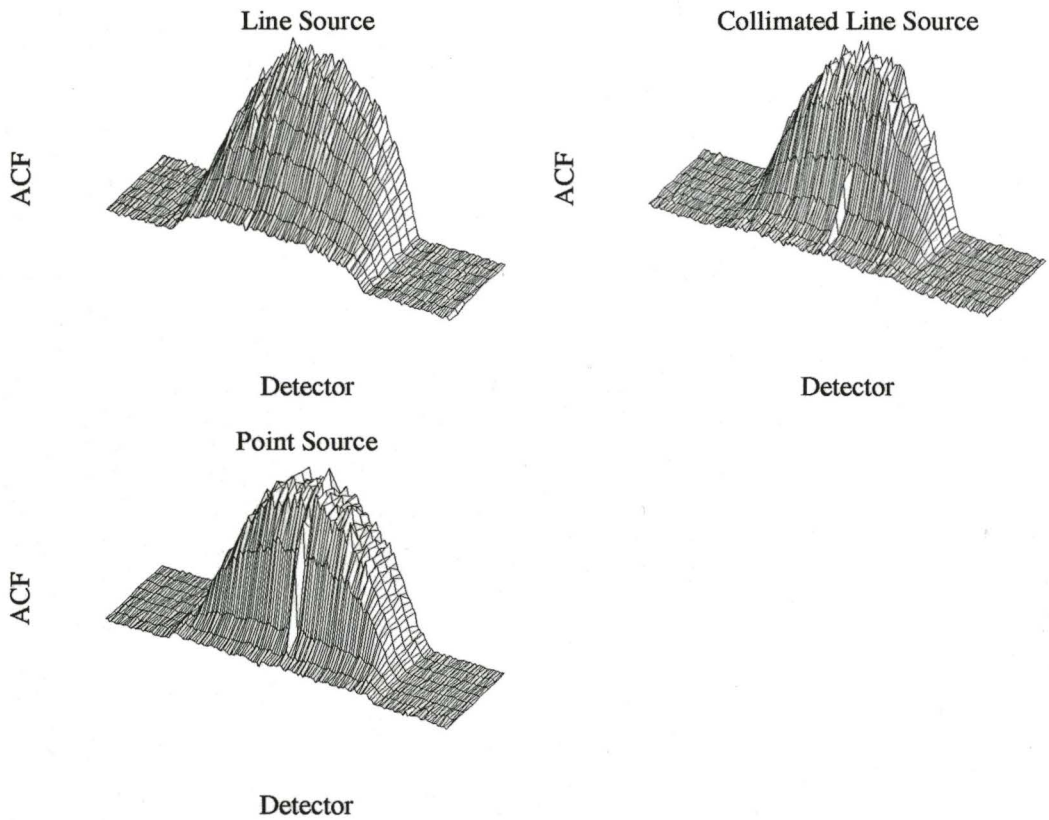

Figure 17 - Axial resolution profiles obtained with various source configurations. An uncollimated line source yields a 4 cm FWHM resolution. With crude collimation this decreases to 2.5 cm. A 1 cm long point source produces 1.5 cm resolution.

Energy Spectra

The energy spectra are shown for blank and 21 cm flood transmission scans in Figure 18. The ring source spectrum does not change noticeably between blank and transmission. With the rod source there is considerable variation in the bucket spectra depending on the location with respect to the source.

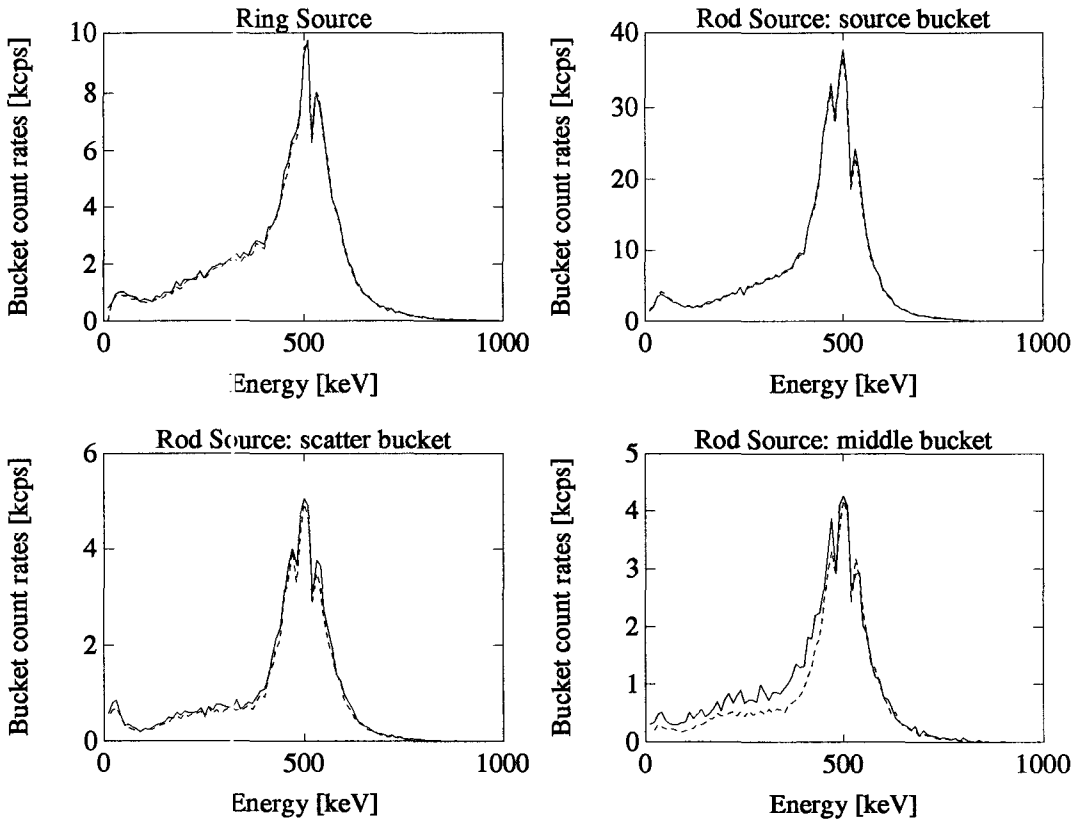

Figure 18 - Energy spectra of blank (dashed) and 21 cm cylinder (solid) transmission scans. The source bucket is next to the rod source. The middle and scatter buckets project through the middle and adjacent to the cylinder respectively.

The rod source spectrum of the bucket next to the source (source bucket), is very close to that of the ring source for both blank and transmission. The middle bucket projects through the centre of the phantom, while the scatter bucket does not project through the phantom at all, but it is still in the FOV. The blank spectra of the scatter bucket and middle bucket are both similar and both have less scatter component (100-400 keV) than the ring source. The scatter bucket transmission spectrum has much less scatter in the range from 200 to 400 keV than the ring source spectrum. The scatter in the middle bucket transmission spectrum is only marginally lower than in the ring source spectrum.

CHAPTER IV

Analysis of Singles Transmission

Many tests were carried out to determine the performance of the singles transmission scanning technique as described in Chapter III. The results were comparable to coincidence transmission scanning in terms of transaxial resolution and response to materials of different density. There were differences in two major tests. The first is count rate which affects the resulting image noise. The second is axial resolution which affects the quantitative accuracy of the corrected images. Other differences were observed in terms of scatter and randoms in the measured counts.

Disadvantages

There are several disadvantages of using singles scanning. The most important of these is a decrease in axial resolution. The technique is also currently very slow and counts at a low efficiency. This precludes the use of this method in a clinical environment without further hardware and software development. There seems to be a strong dependence of the measured attenuation factors on the axial extent of the transmission source, although it does not appreciably degrade the uniformity of the

transmission images.

Axial Resolution

The major disadvantage is a sacrifice in axial resolution. In coincidence mode the transaxial planes are collimated electronically, i.e. a direct tomographic plane is defined by the LORs connecting detectors in the same physical ring. Cross planes are also defined in between the physical planes, by LORs which connect detectors in adjacent rings.

There are fewer tomographic planes created in singles transmission scanning because there are no cross planes. Measurements can only be made at the physical detectors corresponding to the direct planes. Furthermore, there is no electronic collimation of these direct planes. The axial resolution is determined by the collimating septa between detector rings, and by the axial collimation of the transmission source. This problem is not apparent in the transaxial direction because the extent of the source is small in this plane, whereas in the axial direction the source extent is relatively large.

An axially thin point source can produce a resolution equal to the detector width. In the McMaster tomograph the axial detector width is 0.675 cm. A 1 cm long point source produced an axial resolution of approximately 1.5 cm as shown in Figure 17. This equals roughly the source width plus the detector width, so this is

not expected to be the minimum axial resolution obtainable. A point source can only be used to scan only one direct plane at a time, and so has less practical value than a collimated rod source.

The 20 cm rod source produced a very poor axial resolution, while a crudely collimated rod source showed significant improvement to 2.5 cm. However, this is still quite large. Currently, axial smoothing of the transmission scans is performed with an 11 mm Gaussian filter, so the resolution of the raw transmission data should not be lower than this. We conclude that a narrowly collimated beam of photons is necessary to achieve suitable axial resolution, if all physical planes are measured simultaneously. If only one plane is measured at a time, then an axially thin point source can be used.

Underestimated Correction Factors

In singles mode, the measured ACFs are typically underestimated in 20 cm to 30 cm objects by 5-10% as shown in Figure 13. The underestimation is caused by the nonlinear bucket singles response and the acceptance of events which are scattered across planes. The ACFs may be adjusted by correcting the bucket response to be linear with activity, before the dead time correction is applied.

The scatter can be reduced by using a point source or a narrowly collimated rod source, which is closer to the desired narrow beam geometry. This effect is evident in Figure 13, where the 12 cm phantom profile is accurately measured with a point

source. In Figure 12 the attenuation coefficient of the 12 cm water cylinder measured with an uncollimated rod source is 0.080 [cm^{-1}], which is 15% too low. The same effect is evident in the 21 cm phantom images. In Figure 12 μ=0.076 [cm^{-1}] when water is measured with the 20 cm rod source, while in Figure 14 μ=0.084 [cm^{-1}] when measured with a 2 cm point source.

The in-plane scatter is assumed to be similar to that measured when using a rod source in coincidence mode. Scatter does not have a large effect on the transaxial image uniformity. Images of the 21 cm phantoms in Figures 12 and 14 show no noticeable change in uniformity when measured with a 20 cm rod source or a 2 cm point source respectively.

For a given imaging geometry there is a satisfactory response to object density, as shown in Table 5. Therefore a single scaling factor can be determined for brain imaging. This factor is simply the ratio of the measured attenuation coefficient of water divided by the known linear attenuation coefficient. The variance of the error in this correction is equal to the variance in the sizes of scanned brains.

Speed

The speed of the method is the only factor which prevents this technique from being tested clinically. The software written to acquire singles scans cannot run in real time, and takes approximately 12 hours to record what is actually a 64 minute

acquisition.

The low efficiency value of 25% at 2 mCi (as shown in Figure 9) is due to the nature of the hardware and software used to acquire this data. It was designed for maintenance purposes only and has a very high counting dead time. The block dead time value of 0.175 ms presents a count rate limit of 90 cps/detector at saturation, i.e.

1/0.000175 [cps/block] / 64 [detectors/block]

It is necessary to have this count rate with little or no dead time being sorted into sinograms in real time, in order to have suitable performance.

Advantages

There are several advantages realized when using singles transmission for attenuation correction in PET. The signal to noise ratio of measured attenuation factors increases dramatically compared to coincidence transmission measurement. Noise equivalent counts can be used to evaluate the transmission scan quality as described in eq.(23). Recall that the SNR of a reconstructed image increases as the number of true recorded events increases. The SNR decreases as the proportion of randoms and scattered events increases. In singles mode the trues count rate increases dramatically over coincidence mode acquisitions, and there are no randoms. There is increased cross-plane scatter which reduces the image quality slightly, and causes ACF underestimation.

Count Rates

The major benefit comes from the increased count rate of singles scanning at higher source strengths. If there is too much activity in the source, the coincidence transmission efficiency decreases severely because the dead time losses of the near block are very high. However, the efficiency of the opposing block is still relatively high, enabling many more singles to be counted than coincidence events.

The SNR of the method was analyzed using the decaying source data of Figure 9, and the resulting transmission images shown in Figure 12. The results are summarized in Table 6. It is assumed in this analysis that the data quality is dependent only on the transmission scan and not the blank scan. The blank scan has a higher average count rate than the transmission scan and can be performed for a longer time, for example overnight when the tomograph is not in use. It is therefore possible to acquire blank scans which are practically free of noise.

The singles count rate of a blank scan is close to 60 cps/detector with 2 mCi in a collimated rod source as shown in Figure 9. The total count rate of any LOR in the resulting sinogram is twice this rate because there are two contributing detectors to each line of response. At this source strength only 25% of all incident photons are recorded.

TABLE 6

MEASURED AND PREDICTED PERFORMANCE OF SINGLE PHOTON ATTENUATION CORRECTION.

Scan Type (rod source)	Time [min]	Counts* per LOR	Dead Time Corrected	Counting Efficiency	Noise [%]
2 mCi Singles (measured)	64	1200	6000	0.2	1.34
2 mCi Coincidence (measured)	64	650	800	0.8	2.41
20 mCi Real time Singles (predicted)	1.6	700	1000	0.7	1.8

*Counts are average values in unattenuated regions of the transmission scans.

The 21 cm phantom image shown in Figure 12 has a count rate of 120 cps/LOR in an unattenuated (blank) region of the transmission scan. A transmission scan with 1200 measured counts per LOR in an unattenuated region, produced an image with approximately 1.3% noise as shown in Table 6. This was obtained with an uncollimated rod source and a 10 s count at each detector, i.e. 1200 counts/LOR = 60 cps/detector · 10 s/detector · 2 detectors/LOR The average efficiency of this singles acquisition was approximately 20%, at a mean source strength of 2 mCi. The lower efficiency value is due to the increased true count rate with an uncollimated source, as opposed to the collimated data of Figure 9 which shows an efficiency value of 25% at 2 mCi.

A coincidence scan of the 21 cm phantom was also performed using a rod source with 2 mCi of activity. The average unattenuated count per LOR in this scan was 650 counts, and the resulting image noise was 2.4%. The dead time losses in this acquisition were approximately 20% and so, contributed slightly to the variance in the recorded counts.

The image noise varies proportionally with the standard deviation of the measured counts (Strother 1990). At 2 mCi we observe a measured count rate increase of 200% with singles scanning over coincidence scanning, even with significant singles dead time losses of 80%. Using the data in Table 6 and the variance estimation of eq.(20), one would expect to observe a decrease in the percent image noise by a factor of 1.37. This would produce an image with 1.76% noise (2.41% / 1.37), whereas the actual singles image noise is lower than this at 1.34%.

With singles scanning, the dead time corrected count rate of a 2 mCi uncollimated rod source is 600 cps/LOR, while the comparable coincidence rate is 80 cps/LOR. This is a count rate increase of a factor of 7.5 at 2 mCi. The benefit is even greater at higher source strengths because the coincidence counting efficiency decreases much faster than the singles efficiency. Ideally, the source should be mounted closer to the detectors to increase the size of the patient aperture. In this case the count rate increase is even greater; the coincidence efficiency decreases markedly due to the large dead time losses of the adjacent detector, whereas the singles dead time losses are not noticeably affected.

No Randoms

Randoms increase as the product of the detector singles rates along a given LOR as given by eq.(12). If the transmission source strength is doubled, the randoms rate increases by a factor of four, since each of the detector singles rates increases linearly with activity. The randoms fraction, however, does not increase at this rate due to the increase in true counts as well as dead time losses. As the coincidence count rate approaches saturation, the randoms fraction can be a factor of 2 or more. A randoms fraction of 1.0 decreases the NEC by a factor of 2, and the resulting image noise by $\sqrt{2}$. Typical randoms fractions are only around 0.05 for rod transmission scans with a source strength of 5 mCi. Random coincidences result only from coincidence counting, whereas there are no randoms with the singles transmission technique. With under 5 mCi in the rod source, the noise reduction is not significant due to reduced randoms. However, the reduction is more significant if the source strength is increased.

Image Noise

The increased count rate results in images with greater uniformity. This must be traded off against both imaging time and desired strength of the transmission source which affects the patient exposure. If the dead time losses are low then the image noise will vary as the root of both acquisition time and source strength. With singles scanning the source strength can be increased beyond that which is practical with

coincidence scanning, to obtain even further increases in count rate.

Currently the increased count rate of singles scanning reduces the transmission image noise by a factor of two (1.3% versus 2.4%), with a 2 mCi rod source. This factor is larger for a higher activity source, and there is also additional benefit due to reduced randoms at higher source strengths. With 2 mCi in the rod source, the opposing detectors counting efficiency is still approximately 94%, whereas the coincidence efficiency is 80% and the singles counting efficiency is only 20%. This means that further gains are possible if the singles counting dead time is reduced. If the singles counting efficiency is to be improved, hardware implementation of the technique is necessary to record singles in real time.

Practical Potential

Currently the use of singles transmission measurement is not practical because of the low speed of the acquisitions. Even with low counting efficiency, the transmission image noise is improved compared to coincidence scanning. There is a decrease in axial resolution which must be addressed.

Real Time Acquisition

Emission scans are acquired in real time by dedicated hardware. A similar

configuration is necessary to count singles for transmission measurement. This hardware would have to incorporate the spatial resampling in real time as well. A dead time correction algorithm would also be necessary for singles mode acquisitions. Currently, the dead time correction is modelled on measured coincidence count rates. The model includes direct measurement of the hardware live time as well as the randoms and multiples count rates. The maximum count rate which can be generated from the entire tomograph is currently 4 million cps (Dent 1986). This is also the absolute maximum rate at which singles can be recorded if the current hardware is used with the rod source (Jones 1992).

Transmission Quality

A 2 mCi collimated source currently counts at 25% efficiency because of dead time losses as shown in Figure 9. Without dead time, the count rate is 200 cps/detector. Therefore for 160 detectors in 8 planes, the total count rate is approximately 0.25 million cps, which is well below the maximum sorting rate. The detector dead time at this rate is only 6%.

Using the 2 mCi singles data in Table 4, approximately 1000 measured raw counts/LOR are required to produce an image with 1.5% noise. If the rod source strength is increased to 20 mCi and the singles are acquired with little dead time, the corrected count rate becomes 2000 cps/detector (assuming a linear increase from the 2 mCi measurement). Therefore, a 0.25 s count per detector gives 500 counts/detector

· 2 detectors/LOR = 1000 counts/LOR. The total scan time when operating at this rate is 0.25 s/detector · 384 detectors/revolution = 96 s/revolution (1.6 minutes). Eight planes are acquired simultaneously in each ring. This is a substantial improvement over the current image quality of 5% noise in 30 minute coincidence scans.

If the dead time is significant with a high rod source strength, the image noise will increase inversely as the root of the counting efficiency, as given in eq.(20). An example is shown in Table 4 for a collimated 20 mCi rod source. The detector dead time losses have been measured as 30% at 20 mCi. Therefore the noise will increase by a factor of $1 / \sqrt{0.7}$. The resulting noise in the transmission image with 700 counts/LOR would then be 1.5·1.2 = 1.8%.

Axial Resolution

Axial resolution of the transmission scans should be a small as possible. The axial resolution of the singles transmission scans does not have to be reduced to the 6 mm performance of the coincidence transmission technique, because these scans are smoothed with an 11 mm Gaussian filter anyway. Based on the results of the crudely collimated rod source, suitable axial resolution may be possible with a well collimated source. This will enable simultaneous scanning of 8 planes per ring of detectors. Collimator design is not a simple matter, therefore suitable simulation should be performed to determine possible experimental configurations.

Collimation may be improved by using a source of lower energy since 511 keV coincidence events are not specifically required. Since attenuation varies as $E_{\gamma}^{3.5}$ significant gains would be realized. Transmission scans would then have to be calibrated in order to convert from attenuation at a lower energy to attenuation of 511 keV photons which occurs during emission scanning.

Three Dimensional Acquisition

A recent advance in positron tomography designed to increase the counting efficiency is referred to as 3 dimensional acquisition. In this case the septa between the detector rings are removed, enabling many more LORs to be measured between the detector rings. The number of recorded counts per unit of injected dose increases. The net result is simply images which have more counts and therefore less noise. Measurement of the transmission of photons along all these LORs is difficult because of the high randoms rates (McKee 1991). The singles rates are also increased dramatically, therefore singles transmission scanning with a point source may provide a means of measuring attenuation along all possible LORs.

Conclusions

Singles transmission measurement can be used to generate attenuation correction data of higher quality than that obtained with coincidence measurement. The principal advantage is a five- to ten-fold increase in count rate, with a 2 mCi rod transmission source. This is due to lower dead time losses which result with singles versus coincidence acquisitions. The major trade-off is a loss of axial resolution of up to a factor of four. Source collimation is crucial in order to produce acceptable axial resolution, and to reduce cross-plane scatter. Since there are no randoms when counting singles, the source strength can be increased beyond that which is practical with coincidence transmission measurement. Counts can not be windowed to remove in-plane scatter or emission data, as they can with coincidence acquisition. The performance of singles transmission is similar to coincidence measurement in terms of transaxial resolution and response to object density. There is some underestimation of the correction factors for larger objects. This is caused by cross-plane scatter and the nonlinear bucket singles response, which is used in the dead time correction. Implementation of this technique with additional hardware and software is necessary to acquire singles scans in real time with low dead time losses. This will reduce the transmission scanning time to under two minutes, and will produce transmission images with under 2% noise.

APPENDIX A

Singles Acquisition Software

The VAX GANTRY program is used to acquire all data, and the resulting histograms must currently be saved as text files. Therefore for a single ring scan, 384 x 4 files are saved. Each file contains data for a given block on the 7 buckets required to assemble a fan for the given rod position, i.e. 8x8 detectors times 7 buckets in each file, and four files per rod location. The file names indicate the data contained therein, e.g. filename_sn1.96 contains block1 data for the 7 opposing buckets when the rod is at detector 96.

A second program (SINGSCAN.C) which runs on the SUN, then reads all of these files and assembles a coincidence sinogram, using the fan beam for each rod location. This program requires two sets of files; a BLANK scan set and a TRANSMISSION scan set.
The sinogram is computed as the ratio of BLANK / TRANSMISSION. This sinogram can then be smoothed and/or backprojected using the standard ECAT processing tools.

```
$!          singscan.com
$!
$!          define log ecat$sing_scan "busy"
$!          select block 0..3 (s0,s1,s2,s3)
$!          select posit/time histogram and clear histo RAM (h1)
$!          start 150 s histogram (h150) for each block
$!          define log ecat$sing_scan "done"
$!
$           on CONTROL_Y then goto done
$           if p1 .eqs. "" then inquire p1 "Singles name"
$           theta = 0
$           ntheta = 384
$!          theta = 97
$!          ntheta = 98
$           define/nolog ecat$sing_scan "BUSY"
$tloop:
$           dtheta = theta + 96
$           if dtheta .ge. 384 then dtheta = dtheta - 384
$           b = 0
$           bucket1 = (dtheta+16) / 32
$           bucket1 = (bucket1 + 3)
$           if bucket1 .gt. 11 then bucket1 = bucket1 - 12
$           write sys$output ""
$           write sys$output "********** THETA = ''dtheta' ->B1 = ''bucket1'"
$           angle = theta*360/384
$           if angle .ge. 360 then angle = angle - 360
$           point = theta*3600000/384 - theta*360/384*10000
$           if point .lt. 1000 then goto fixpoint
$           set ver
$           mov/source='angle'.'point'
$           set nover
$           goto bloop
$fixpoint:
$           set ver
$           mov/source='angle'.0'point'
$           set nover
$bloop:
$           write sys$output "********** POLLING ''dtheta' ->''b' SINGLES"
$           define/user sys$output block.jnk
$           @block'bucket1'.'b'
```

```
$          define/user sys$output ihist.jnk
$          @ihist'bucket1'.com
$          define/user sys$output hist.jnk
$          @hist'bucket1'.com
$          set nover
$          write sys$output '**********  WAITING FOR 10 S HISTOGRAM"
$          wait 00:00:10    ! delay if files exist
$!
$!         bucket2 = bucket1 + 12
$          write sys$output '**********  CHECKING FOR STATUS 'N 0'"
$          gantry
0h0


$          write sys$output '**********  DUMPING SINGLES TO FILE"
$          define/user sys$output ecat$data:'p1'_sn'b'.'dtheta'
$          @sing'bucket1'.com
$          define/user sys$output ecat$data:'p1'_dt'b'.'dtheta'
$          @dead'bucket1'.com
$!
$          b = b + 1
$          if b .lt. 4 then goto bloop
$!
$          theta = theta + 1
$          if theta .lt. ntheta then goto tloop
$done:
$          dtheta = theta + 96
$          define/user sys$output ecat$data:'p1'_dt'b'.last
$          @dead'bucket1'.com
$!
$          purge
$          define/nolog ecat$sing_scan "DONE"
$          exit
$notime:
$          write sys$output '**********  Scan too short for singles acquisition"
$          exit

::::::::::::::
singscan.c
::::::::::::::
char singtfile[40];
char singbfile[40];

void sing_file(det, blank, transm)
int det;
int blank[8][160];
int transm[8][160];
{
FILE *singb, *singt, *bdt, *tdt;
char fname[80];
int i,j,k,b;
int vmin = 10000, vmax = 0;
double counts=0.0;
double bcorrect, tcorrect, histtime = 10.0; /* ten second histograms */
static double bbuf[8][224];
static double tbuf[8][224];
static double bsum[7][4];
static double tsum[7][4];
static double bsums[7][4];
static double tsums[7][4];
static double bbsum[7];
static double ttsum[7];
static double bbdt[7];
static double ttdt[7];
static double bbsumdt[7][4];
static double ttsumdt[7][4];
static short b1,d1;
static short b1_to_d1[12] = {368,16,48,80,112,144,176,208,240,272,304,336};

printf("det = %d; ",det);
```

```
for (b = 0; b < 7; b++) {
        bbsum[b] = 0;
        ttsum[b] = 0;
        bbdt[b] = 0;
        ttdt[b] = 0;
}
for (i = 0; i < 8; i++)
        for (j = 0; j < 224; j++)
                bbuf[i][j] = tbuf[i][j] = 0.0;
                                                        /* read profile of data */
for (i = 0; i < 4; i++) {

        sprintf(fname,"%s_sn%d.%d",singbfile,i,det);
        if ((singb = fopen(fname,"r")) == NULL)
                {printf("singb open err\n"); exit();}
        sprintf(fname,"%s_sn%d.%d",singtfile,i,det);
        if ((singt = fopen(fname,"r")) == NULL)
                {printf("singt open err\n"); exit();}

        sprintf(fname,"%s_dt%d.%d",singbfile,i,det);
        if ((bdt = fopen(fname,"r")) == NULL)
                {printf("singb open err\n"); exit();}
        sprintf(fname,"%s_dt%d.%d",singtfile,i,det);
        if ((tdt = fopen(fname,"r")) == NULL)
                {printf("singt open err\n"); exit();}

        for (b = 0; b < 7; b++) {
                fscanf(singb," %*s %s ",fname);          /* skip $gantry > */
                fscanf(singt," %*s %s ",fname); /* skip $gantry > */
                fscanf(bdt," %*s %s ",fname);
                fscanf(bdt," %*s %lf,%*s ",&counts);
                if (counts < 1.0e6) bbsumdt[b][i] = counts;
                else printf("%s_dt%d.%d in bucket+ %d; ",singbfile,i,det,b);

                fscanf(tdt," %*s %s ",fname);
                fscanf(tdt," %*s %lf,%*s ",&counts);
                if (counts < 1.0e6) ttsumdt[b][i] = counts;
                else printf("%s_dt%d.%d in bucket+ %d; ",singtfile,i,det,b);

                for (j = 0; j < 8; j++)
                for (k = 0; k < 8; k++) {
                        fscanf(singb,"%lf,", &counts);
                        bbuf[j][i*8 + b*32 + (7-k)] += counts / histtime;
                        fscanf(singt,"%lf,", &counts);
                        tbuf[j][i*8 + b*32 + (7-k)] += counts / histtime;
                }
        }
        fclose(singb);
        fclose(singt);
        fclose(bdt);
        fclose(tdt);
}
                                                /* dead time corrected bucket avgs */
/* avg bucket count rate  */
for (b = 0; b < 7; b++) {
    ttdt[b] = 0.0;
    bbdt[b] = 0.0;
    for (i = 0; i < 4; i++) {
        ttdt[b] += ttsumdt[b][i];
        bbdt[b] += bbsumdt[b][i];
    }
    ttdt[b] /= 4;
    bbdt[b] /= 4;
/*    for (i = 0; i < 4; i++) {
        if (fabs(ttdt[b] - ttsumdt[b][i]) > ttdt[b]/10.0)
                printf("check block %d; ", i);
    }
*/
}

                                        /* dead time correct block averages */
```

```
for (i = 0; i < 4; i++) {
/*          printf("\ntransm block tot = ");*/
            for (b = 0; b < 7; b++) {
                        bsum[b][i] = 0.0;
                        tsum[b][i] = 0.0;
                        for (j = 0; j < 8; j++)
                        for (k = 0; k < 8; k++) {
                                    bsum[b][i] += bbuf[j][i*8 + b*32 + (7-k)];
                                    tsum[b][i] += tbuf[j][i*8 + b*32 + (7-k)];
                        }
                        bsums[b][i] = bsum[b][i];
                        tsums[b][i] = tsum[b][i];
                        bsum[b][i] /= (1.0 - bsum[b][i]*0.000175);
                        tsum[b][i] /= (1.0 - tsum[b][i]*0.000175);
            }
            printf("\n");
}
for (b = 0; b < 7; b++) {
            bbsum[b] = 0.0;
            ttsum[b] = 0.0;
            for (i = 0; i < 4; i++) {
                        bbsum[b] += bsum[b][i];
                        ttsum[b] += tsum[b][i];
            }
}


for (i = 0; i < 4; i++) {
            for (b = 0; b < 7; b++) {
                        bcorrect = bbdt[b] / bbsum[b] * bsum[b][i] / bsums[b][i];
                        tcorrect = ttdt[b] / ttsum[b] * tsum[b][i] / tsums[b][i];
/*                      bcorrect = bsum[b][i] / bsums[b][i];
                        tcorrect = tsum[b][i] / tsums[b][i];
*/                      for (j = 0; j < 8; j++)
                        for (k = 0; k < 8; k++) {
                                    bbuf[j][i*8 + b*32 + (7-k)] *= bcorrect;
                                    tbuf[j][i*8 + b*32 + (7-k)] *= tcorrect;
                        }
            }

}

b1 = ((det+16)/32 +3) % 12;
d1 = b1_to_d1[b1];
d1 = ((det+112) % 384) - d1;
if (d1 < 0) d1 += 384;

if (d1 > 64) {
            printf("delta OOR\n");
            exit();
}
else {
            printf("d1= %d\n", d1);
            for (i=0;i<160;i++) {
                for (j=0;j<8;j++) {
                        blank[j][i] = (int)(histtime*bbuf[j][d1]);
                        transm[j][i] = (int)(histtime*tbuf[j][d1]);
                }
                d1++;
            }
}

            /* save raw ACF profiles */
/*          singt = fopen("singmesh.mat","w");
            for (i=0;i<160;i++) {
                        fprintf(singt,"%d\t",1000*blank[7][i]/transm[7][i]);
                        fprintf(singt,"%d\t",1000*blank[6][i]/transm[6][i]);
                        fprintf(singt,"%d\t",1000*blank[5][i]/transm[5][i]);
                        fprintf(singt,"%d\t",1000*blank[4][i]/transm[4][i]);
                        fprintf(singt,"%d\t",1000*blank[3][i]/transm[3][i]);
                        fprintf(singt,"%d\t",1000*blank[2][i]/transm[2][i]);
```

```
                fprintf(singt,"%d\t",1000*blank[1][i]/transm[1][i]);
                fprintf(singt,"%d\t\n",1000*blank[0][i]/transm[0][i]);
        }
        fclose(singt);
*/
}

#define DET 7
main(argc, argv)
int argc;
char *argv[];
{               /* Start of MAIN Routine        */
        FILE *singp;
        int i,j, lastd1=-1, d1=-1, d2, a,r, oneproj=-1;
        int startdet1=216, enddet1=408, startdet2=24, enddet2=216;
        int blank[8][160];
        int transm[8][160];
        char outname[40]  varname[10];
        FILE *fp1, *fp2, *fp3, *mat_create();
        char *pname, sino_filename[40];
        double deld1[160], d1p, nextd1p, rp, nextrp, a1, a2, x, y, ad;
        double pi=3.1415, radius=38.0, w1, w2;
        static short *sino_buf1, max_val1;
        static short *sino_buf2, max_val2;
        static float *profile, scaler;
        static Main_header mhead;
        static struct MatDir entry, matrix_list[60];
        static Scan_subheader sc_head1, sc_head2;
        static int mat_num, mat_frame=1, mat_plane=1, mat_gate=1, mat_data=0, mat_bed=0, num_mat=0, num_matrices=0;
        static int data_type=2, nprojs, nviews, nplanes=1;

/*      Check number of input variables */
        {
                if ((argc--)>0) pname=(*(argv++));
                if ((argc--)>0) strcpy(singbfile,(*(argv++)));
                if ((argc--)>0) strcpy(singtfile,(*(argv++)));
                if ((argc--)>0) sscanf( (*(argv++)),"%d", &oneproj);
        }
        printf("transm = %s_sn%d.%d\n",singtfile,0,oneproj);
        if (oneproj != -1) {
                if (oneproj > startdet2 && oneproj < enddet2) {
                        startdet2 = oneproj;
                        enddet2 = oneproj+1;
                        startdet1 = 0;
                        enddet1 = 0;
                }
                else {
                        startdet1 = oneproj;
                        enddet1 = oneproj+1;
                        startdet2 = 0;
                        enddet2 = 0;
                }
        }

/*      Open sinogram file */
        fp1=mat_open("onesino.scn", "r");

/*      Read main header block of sinogram file */
        mat_read_main_header(fp1, &mhead);
        num_matrices=mat_list(fp1, matrix_list, 60);
        if(!num_matrices)
                errtxt("\n\tNo matrices found in Sinogram File\n");

        sprintf(sino_filename,"%s","singb.scn");
        fp2=mat_create(sino_filename, &mhead);
        sprintf(sino_filename,"%s","singt.scn");
        fp3=mat_create(sino_filename, &mhead);


          /* Get matrix number */
                mat_num=mat_numcod(mat_frame, mat_plane, mat_gate, mat_data, mat_bed);
```

```
/* Locate, read blank sinogram file header information */
        mat_lookup(fp1, mat_num, &entry);
        mat_read_scan_subheader(fp1, entry.strtblk, &sc_head1);
        mat_read_scan_subheader(fp1, entry.strtblk, &sc_head2);
/* Read blank sinogram data */
        if(!sinc_buf1) sino_buf1=(short*)calloc(sc_head1.dimension_1*sc_head1.dimension_2*sizeof(short),1);
        if(!sinc_buf2) sino_buf2=(short*)calloc(sc_head2.dimension_1*sc_head2.dimension_2*sizeof(short),1);

/* calculate d1 offsets for each d2 in a fan */
        for (i=0; i < 160; i++) {
                a1 = pi*2.0/384.0*(i-80);
                y = radius*sin(a1);
                x = radius*cos(a1) + 24.0;
                a2 = atan(y/x);
                ad = 2.0*a2 - a1;
                deld1[i] = ad*192/pi;
        }

        singp = fopen("singprof.mat","w");
        if (oneproj != -1) for (i=0;i<24;i++) fprintf(singp,"0\t\n");

/* create singles sino */
        for (i=startdet1; i < enddet1; i++) {
                d1 = i;
                sing_file((i%384), blank,transm);
                d2 = (d1+112);
                for (j=0; j < 159; j++) {
                        d1 = (int)(deld1[j] + 0.5 + i);
                        a = ((d1-216) + (j+1)/2);

                        d1p = deld1[j] + i;
                        nextd1p = deld1[j+1] + i;
                        if ((int)d1p == (int)nextd1p) {
                                rp = d2 - d1p - 112;
                                nextrp = d2 - nextd1p - 111;

                                r = d2 - (int)d1p - 112;
                                if (r < 0 || r >= 160)
                                        {printf("r OOR\n");exit();}
                                if (a > 191) {
                                        a -= 192;
                                        r = 159-r;
                                }
                                if (a < 0) {
                                        a += 192;
                                        r = 159-r;
                                }
                                w1 = (rp-(int)rp);
                                w2 = (1.0-nextrp+(int)nextrp);
                                sino_buf1[(a%192)*160+r] +=
                                        ((w2*blank[DET][j] + w1*blank[DET][j+1]) / (w1+w2) / 5);
                                sino_buf2[(a%192)*160+r] +=
                                        ((w2*transm[DET][j] + w1*transm[DET][j+1]) / (w1+w2) / 5);
if (oneproj != -1) {
        fprintf(singp,"%d\t\n",1000L*sino_buf1[(a%192)*160+r]/sino_buf2[(a%192)*160+r]);
}
                        }
                        d2++;
                }
        }
        for (i=startdet2; i < enddet2; i++) {
                d1 = i;
                sing_file((i%384), blank,transm);
                d2 = (d1+112);
                for (j=0; j < 159; j++) {
                        d1 = (int)(deld1[j] + 0.5 + i);
                        a = ((d1-24) + (j+1)/2);

                        d1p = deld1[j] + i;
                        nextd1p = deld1[j+1] + i;
                        if ((int)d1p == (int)nextd1p) {
```

```
                                        rp = 159.0 - (d2 - d1p - 112);
                                        nextrp = 159.0 - (d2 - nextd1p - 111);

                                        r = 159 - (d2 - (int)d1p - 112);
                                        if (r < 0 || r >= 160)
                                                {printf("r OOR\n");exit();}
                                        if (a > 191) {
                                                a -= 192;
                                                r = 159-r;
                                        }
                                        if (a < 0) {
                                                a += 192;
                                                r = 159-r;
                                        }
                                        w1 = (rp-(int)rp);
                                        w2 = (1.0-nextrp+(int)nextrp);
                                        sino_buf1[(a%192)*160+r] +=
                                                ((w2*blank[DET][j] + w1*blank[DET][j+1]) / (w1+w2) / 5);
                                        sino_buf2[(a%192)*160+r] +=
                                                ((w2*transm[DET][j] + w1*transm[DET][j+1]) / (w1+w2) / 5);
        if (oneproj != -1) {
                fprintf(singp,"%d\t\n",1000L*sino_buf1[(a%192)*160+r]/sino_buf2[(a%192)*160+r]);
        }
                                        }
                                        d2++;
                                }
                        }
                        max_val1 = 0;
                        max_val2 = 0;
                        for (i = 0; i < 192*160; i++) {
                                if (max_val1 < sino_buf1[i]) max_val1 = sino_buf1[i];
                                if (max_val2 < sino_buf2[i]) max_val2 = sino_buf2[i];
                        }
                        sc_head1.scan_max = max_val1;
                        sc_head2.scan_max = max_val2;
OUTPUT:
          /* write sino buf */
                        mat_write_scan(fp2, mat_num, &sc_head1, sino_buf1, 192*160*sizeof(short));
                        mat_write_scan(fp3, mat_num, &sc_head2, sino_buf2, 192*160*sizeof(short));

  /* Deallocate memory */
        free(sino_buf1);
        free(sino_buf2);

/*      Close open files */
        mat_close(fp1);
        mat_close(fp2);
        mat_close(fp3);

        if (oneproj != -1) for (i=0;i<23;i++) fprintf(singp,"0\t\n");
        fclose(singp);

}               /* End of MAIN Routine                  */
```

APPENDIX B

Measured Data

Image ROIs used to evaluate attenuation coefficients

::::::::::::::

sing175_roi.cpt; 21 cm water cylinder transmission image reconstructed with block dead time of 0.175 ms.

::::::::::::::

In units of ECAT counts per pixel per second

Matrix: 1 1 1 0 0

ROI ID	ROI Avg	#pixels (screen)	ROI Total	%Stdev	ROI Min.	ROI Max.	ROI Surf. mmxmm	ROI Vol. mmxmmxmm
1	7.5566e-02	1541	2.9112e+01	3.4	6.7755e-02	8.1536e-02	1.4545e+03	4.9089e+03
2	7.4698e-02	1541	2.8777e+01	3.2	6.9185e-02	8.1198e-02	1.4545e+03	4.9089e+03
3	7.4883e-02	1541	2.8849e+01	3.9	6.6436e-02	8.5380e-02	1.4545e+03	4.9089e+03
4	7.5725e-02	1541	2.9173e+01	3.2	6.8453e-02	8.2313e-02	1.4545e+03	4.9089e+03
5	7.5543e-02	1541	2.9103e+01	3.1	6.8808e-02	8.0968e-02	1.4545e+03	4.9089e+03
6	7.5510e-02	1541	2.9090e+01	2.9	6.9894e-02	8.2099e-02	1.4545e+03	4.9089e+03
7	7.6059e-02	1541	2.9302e+01	3.0	7.0593e-02	8.1815e-02	1.4545e+03	4.9089e+03
8	7.5458e-02	1541	2.9070e+01	2.5	6.9949e-02	8.1023e-02	1.4545e+03	4.9089e+03
9	7.6460e-02	1541	2.9456e+01	3.1	6.9118e-02	8.3285e-02	1.4545e+03	4.9089e+03
10	7.6281e-02	1541	2.9387e+01	3.1	6.9876e-02	8.2578e-02	1.4545e+03	4.9089e+03

::::::::::::::

sing175s_roi.cpt; smoothed 21 cm water cylinder transmission image reconstructed with block dead time of 0.175 ms.

::::::::::::::

In units of ECAT counts per pixel per second

Matrix: 1 1 1 0 0

ROI ID	ROI Avg	#pixels (screen)	ROI Total	%Stdev	ROI Min.	ROI Max.	ROI Surf. mmxmm	ROI Vol. mmxmmxmm
1	7.6062e-02	1541	2.9303e+01	1.2	7.3928e-02	7.7803e-02	1.4545e+03	4.9089e+03
2	7.5189e-02	1541	2.8967e+01	1.6	7.1927e-02	7.7533e-02	1.4545e+03	4.9089e+03
3	7.5352e-02	1541	2.9029e+01	2.2	7.1627e-02	7.9695e-02	1.4545e+03	4.9089e+03
4	7.6128e-02	1541	2.9328e+01	1.3	7.3247e-02	7.8345e-02	1.4545e+03	4.9089e+03
5	7.6087e-02	1541	2.9312e+01	1.3	7.3449e-02	7.8034e-02	1.4545e+03	4.9089e+03
6	7.5958e-02	1541	2.9263e+01	1.2	7.3026e-02	7.8364e-02	1.4545e+03	4.9089e+03
7	7.6507e-02	1541	2.9474e+01	0.9	7.5264e-02	7.8097e-02	1.4545e+03	4.9089e+03
8	7.5882e-02	1541	2.9233e+01	1.1	7.3948e-02	7.8056e-02	1.4545e+03	4.9089e+03
9	7.6883e-02	1541	2.9619e+01	1.5	7.4103e-02	7.8744e-02	1.4545e+03	4.9089e+03
10	7.6665e-02	1541	2.9535e+01	1.1	7.5020e-02	7.8795e-02	1.4545e+03	4.9089e+03

::::::::::::::

singal4sw_roi.cpt; smoothed 21 cm density phantom transmission image of plane 4, (water regions).

::::::::::::::

In units of ECAT counts per pixel per second

Matrix: 1 1 1 0 0

ROI ID	ROI Avg	#pixels (screen)	ROI Total	%Stdev	ROI Min.	ROI Max.	ROI Surf. mmxmm	ROI Vol. mmxmmxmm
1	8.2657e-02	1541	3.1844e+01	2.8	7.7185e-02	8.8553e-02	1.4545e+03	4.9089e+03
2	8.3557e-02	1541	3.2190e+01	2.9	7.8022e-02	8.8829e-02	1.4545e+03	4.9089e+03
3	8.3220e-02	1541	3.2061e+01	2.6	7.8277e-02	8.8553e-02	1.4545e+03	4.9089e+03
4	8.4716e-02	1541	3.2637e+01	1.9	8.0655e-02	8.9349e-02	1.4545e+03	4.9089e+03
5	8.5523e-02	1541	3.2948e+01	2.6	8.0104e-02	9.2018e-02	1.4545e+03	4.9089e+03
6	8.7002e-02	1541	3.3517e+01	2.9	8.0218e-02	9.2627e-02	1.4545e+03	4.9089e+03
7	8.5496e-02	1541	3.2937e+01	2.9	7.9609e-02	9.0785e-02	1.4545e+03	4.9089e+03
8	8.4753e-02	1541	3.2651e+01	2.8	7.8860e-02	9.1997e-02	1.4545e+03	4.9089e+03
9	8.4884e-02	1541	3.2702e+01	2.2	7.7845e-02	9.0837e-02	1.4545e+03	4.9089e+03
10	8.4468e-02	1541	3.2541e+01	2.4	7.9224e-02	8.9796e-02	1.4545e+03	4.9089e+03

::::::::::::::
singal4_roi.cpt; 21 cm density phantom transmission image of plane 4. (air, Al, water = ROI 1,2,3)
::::::::::::::
In units of ECAT counts per pixel per second
Matrix: 1 1 1 0 0

ROI ID	ROI Avg	#pixels (screen)	ROI Total	%Stdev	ROI Min.	ROI Max.	ROI Surf. mmxmm	ROI Vol. mmxmmxmm
1	2.6060e-02	57	3.7136e-01	10.0	2.2872e-02	3.3571e-02	5.3800e+01	1.8157e+02
2	1.8394e-01	57	2.6211e+00	3.4	1.6402e-01	1.9221e-01	5.3800e+01	1.8157e+02
3	8.2789e-02	1153	2.3864e+01	5.4	6.6674e-02	9.2490e-02	1.0883e+03	3.6729e+03

::::::::::::::
singal4s_roi.cpt; smoothed 21 cm density phantom transmission image of plane 4. (air, Al, water = ROI 1,2,3)
::::::::::::::
In units of ECAT counts per pixel per second
Matrix: 1 1 1 0 0

ROI ID	ROI Avg	#pixels (screen)	ROI Total	%Stdev	ROI Min.	ROI Max.	ROI Surf. mmxmm	ROI Vol. mmxmmxmm
1	3.8982e-02	57	5.5549e-01	4.9	3.6576e-02	4.4433e-02	5.3800e+01	1.8157e+02
2	1.6629e-01	57	2.3697e+00	1.7	1.6080e-01	1.7048e-01	5.3800e+01	1.8157e+02
3	8.4095e-02	1153	2.4240e+01	1.6	8.0031e-02	8.7705e-02	1.0883e+03	3.6729e+03

::::::::::::::
singr0_roi.cpt; 12 cm off-centre water cylinder transmission image of plane 0.
::::::::::::::
Matrix: 1 1 1 0 0

ROI ID	ROI Avg	#pixels	ROI Total	%Stdev	ROI Min.	ROI Max.	ROI Surf. mmxmm	ROI Vol. mmxmmxmm
2	7.8123e-02	213	1.6640e+01	2.8	7.2648e-02	8.4006e-02	8.0416e+02	2.7141e+03
3	7.8397e-02	213	1.6699e+01	2.2	7.4050e-02	8.1773e-02	8.0416e+02	2.7141e+03
4	7.7187e-02	213	1.6441e+01	3.7	6.9249e-02	8.3830e-02	8.0416e+02	2.7141e+03
5	7.7792e-02	213	1.6570e+01	3.6	7.2096e-02	8.3593e-02	8.0416e+02	2.7141e+03
6	7.7600e-02	213	1.6529e+01	3.6	7.1502e-02	8.4579e-02	8.0416e+02	2.7141e+03

Dead Time Estimates [ns]

Blocks within one bucket: 0.1693, 0.1737, 0.1803, 0.1887. avg = 1.78, σ = 0.008
Blocks in different buckets: 0.197, 0.150, 0.171, 0.178. avg = 1.74, σ = 0.019

REFERENCES

Barrett H.H., 1984, The Radon Transform and Its Application. In: Progress in Optics XXI E.Wolf (ed.).

Bergstrom M., Ericson K., Bohm C., et al., 1980, Corrections for attenuation, scattered radiation, and random coincidences in a ring detector positron emission transaxial tomograph. IEEE Trans.Nucl.Sci. **27** p.549.

Bergstrom M., Eriksson L., Bohm C., et al., 1983, Correction for Scattered Radiation in a Ring Detector Positron Camera by Integral Transformation of the Projections. JCAT **7** p.42.

Brownell G.L., Sweet W.H., 1953, Localization of Brain Tumors with Positron Emitters. Nucleonics, **11** p.40.

Cahoon J.L., Huesman R.H., Derenzo S.E., et al., 1986, The Electronics for the Donner 600-crystal Positron Tomograph. IEEE Trans.Nucl.Sci. **33** p.570.

Carroll L.R., Kretz P., Orcutt G., 1983, The orbiting rod source: Improving performance in PET transmission correction scans. In: Emission Computed Tomography: Current Trends. Society of Nuclear Medicine, p.235.

Carson R.E., Daube-Witherspoon M.E., Green M.V., 1988, A Method for Postinjection PET Transmission Measurements with a Rotating Source. JNM **29** p.1558.

Dahlbom M., Hoffman E.J., 1987, Problems in Signal-to-Noise Ratio for Attenuation Correction in High Resolution PET. IEEE Trans.Nucl.Sci. **34** p.288.

Dent H.M., Jones W.F., Casey M.E., 1986, A Real Time Digital Coincidence Processor for Positron Emission Tomography. IEEE Trans.Nucl.Sci. **33** p.556.

Derenzo S.E., Zaklad H., Budinger T.F., 1975, Analytical Study of a High-Resolution Positron Ring Detector System for Transaxial Reconstruction Tomography. JNM **16** p.1166.

Digby W.M., Hoffman E.J., 1989, An Investigation of Scatter in Attenuation Correction for PET. IEEE Trans.Nucl.Sci. **36** p.1038.

Evans R.D., 1982, The Atomic Nucleus. New York, McGraw-Hill Book Company, Inc.

Herman G.T.(ed), 1979, Image Reconstruction From Projections. New York, Springer Verlag.

Herman G.T., 1980, Image Reconstruction From Projections. New York, Academic Press.

Johns H.E., Cunningham J.R., 1971, The Physics of Radiology. Springfield, Charles C Thomas Publisher, p.744.

Jones W.M., 1992, Private communication. Knoxville, SIEMENS/CTI.

Kennett T.J., 1992, Private communication. Hamilton, McMaster University.

Knoll G.F., 1989, Radiation Detection and Measurement. New York, John Wiley & Sons.

McKee B.T.A., Clack R., Harvey P.J., et al., 1991, Accurate attenuation correction for a 3D PET system. Phys.Med.Biol. **36** p.603.

Pages L. et al., 1972, Energy Loss of Electrons. Atomic Data **4** p.1.

Michel C., Bol A., De Volder A.G., Goffinet A.M., 1989, Online brain attenuation correction in PET: towards a fully automated data handling in a clinical environment. EJNM **15** p.712.

Rankowitz S., Robertson J.S., Higinbotham W.A., 1962, Positron Scanner for Locating Brain Tumors. IRE International Convention Record, **9** p.49.

Sorenson J.A., Phelps M.E., 1987, Physics in Nuclear Medicine. Philadelphia, W.B.Saunders Company.

Strother S.C., Casey M.E., Hoffman E.J., 1990, Measuring PET Scanner Sensitivity: Relating Countrates to Image Signal-to-Noise Ratios using Noise Equivalent Counts. IEEE Trans.Nucl.Sci. **37** p.783.

Sweet W.H., 1951, Uses of nuclear disintegrations in the diagnosis and treatment of brain tumors. N.E.J.Med. **245** p.875.

Thompson C.J., Ranger N., Evans A.C., Gjedde A., 1991, Validation of Simultaneous PET Emission and Transmission Scans. JNM **32** p.154.

Tomitani T., 1987, An Edge Detection Algorithm for Attenuation Correction in Emission CT. IEEE Trans.Nucl.Sci. **34** p.309.

Webb S., 1988, Emission Computed Tomography. In: The Physics of Medical Imaging, Philadelphia, Hilger.

Wrenn F.W.Jr., Good M.L., Handler P., 1951, The Use of Positron Emitting Radioisotopes for the Localization of Brain Tumors. Science, p.525.